Title: High temperature nanoindentation of iron: experimental and computational study[1]

Authors: T. Khvan[a,b,*], L. Noels[b], D. Terentyev[a], F. Dencker[c], D. Stauffer[d], U.D. Hangen[e], W. Van Renterghem[a], C. Cheng[a], A. Zinovev[a]

[a] - Institute for Nuclear Materials Science, SCK CEN, Boeretang 200, Mol B-2400, Belgium
[b] - Aerospace and Mechanical Engineering Department, University of Liège, B52/3, Quartier Polytech 1, Allée de la Découverte 9, 4000 Liège (Sart Tilman), Belgium
[c] - Institute of Micro Production Technology, Leibniz University Hannover, An der Universitaet 2, 30823 Garbsen
[d] - Bruker Nano Surfaces, Bruker Inc., 9625 West 76th St, Eden Prairie, MN, 55419, USA
[e] - Bruker Nano GmbH, Dennewartstrasse 25, Aachen, 52068, Germany

Journal: JNM

ABSTRACT

Application of reduced activation ferritic/martensitic (RAFM) steels as the structural material in future fusion reactors requires the knowledge of their mechanical properties under relevant operational conditions i.e. temperatures and irradiation by fast neutrons. Execution of the neutron irradiation and post irradiation examination is expensive and lengthy, therefore experimental and computational solutions to ease the characterization of as-irradiated materials are in the scope of interests of nuclear materials scientific community. Moreover, ion irradiation is considered as one possible way to surrogate high flux neutron irradiation damage. The extraction of the mechanical properties after ion irradiation primarily relies on the nanoindentation techniques and its subsequent post processing to extract engineering relevant information, although some innovative techniques such as compression micropillars and micro-tensile testing also exist. In this work, we have performed nanoindentation on BCC iron, as the basis material for ferritic steels, by using a new Bruker stage developed for high temperature operation. The obtained results were analyzed by means of crystal plasticity finite element method (CPFEM), whereas the constitutive laws of the material were derived and established by using tensile deformation data, thus providing an interconnection of material's behavior under compressive and tensile deformations. The microstructural features such as indentation pile-up formation or dislocation density evolution were obtained by using transmission and scanning electron microscopy, and were compared with the predictions derived by the developed CPFEM model. It is demonstrated that a good agreement between the CPFEM and experimental data set, including tensile and compressive loads as well as associated microstructural changes, is obtained at room temperature and elevated temperature tests.

Keywords: high temperature, nanoindentation, CPFEM, iron
* - corresponding author: tymofii.khvan@sckcen.be

1. Introduction:

High Cr ferritic/martensitic (F/M) steels are the primary candidate structural materials for the development of key components in future fusion reactors [1]. A reduced activation ferritic/martensitic (RAFM) steel Eurofer97 was selected as structural material for the first wall and breeding blanket components of fusion reactors [2]. RAFM steel exhibits low neutron-induced swelling, as well as significantly higher thermal conductivity and lower thermal expansion compared to austenitic steels [3].

Fusion reactors will endure harmful operational conditions. The operating temperature of structural steels is expected to be around 550°C if He is used as coolant and around 300°C in the case of water coolant. The irradiation dose over the lifetime of in-vessel components will exceed 50 dpa [4]. Reaching such high irradiation levels in material test reactors is expensive and time consuming. Heavy ion irradiation is an attractive solution to mimic neutron irradiation up to high doses while avoiding problems with activation. The advantage of ion irradiation prior to neutron (in terms of research) is coming from the lesser irradiation time and safer post-irradiation testing. Therefore, a significant part of ongoing nuclear materials sciences research is oriented on surrogating the neutron damage with

ions [5][6], to be, in particular, applied for primary candidates structural materials for future nuclear applications, where neutron doses are especially high. However, ion irradiation generates a very thin damaged layer which requires a tool to assess the modification of mechanical properties after ion irradiation at the appropriate length scale, such as nanoindentation. Another issue which araises in the case of ion irradiation is a non-homogeneous depth damage pattern, and the retrieval of the true mechanical properties requires reverse finite element analysis (FEA) to enable extraction of the hardening induced by the irradiation. The model designing includes parametrization of constitutive law in the relevant temperature range and implementation of microscale irradiation damage effect, in order to predict the impact of the irradiation defects on the material's properties such as yield stress and hardness due to irradiation hardening.

Application of nanoindentation technique in nuclear materials sciences is strongly increasing nowadays due to several aspects:

- It is a non-destructive method allowing to deduce important mechanical properties of materials, such as hardness, elastic modulus or creep and their change after irradiation. Studies show a good prediction of macroscopic tensile properties using nanoindentation [7].
- Nanoindentation requires a very small volume of material for testing, which is an important factor for miniaturization concept in nuclear materials sciences – reduction of specimen dimensions in order to decrease irradiation time and costs as well as post-irradiation activity.
- A compact testing bench can perform a variety of types (depending on indentation tip equipped) and values of mechanical loads; some setups are also able to provide high temperature and post-irradiation testing.

However, one of the most useful application of nanoindentation within the nuclear materials sciences field is an expected possibility to characterize an irradiation impact of several µm ion-irradiated layer, which is located on the subsurface of a material. The use of FEM to simulate nanoindentation process of ion-irradiated SS316 stainless steel in order to analyze the irradiation hardening was demonstrated by Saleh [8], [9]. Another important work was done by Knapp where ion-irradiated layers and thin films implanted to various materials including metals were studied by means of nanoindentation and FEM to deduce the yield stress, hardness and Young's modulus of these layers with a decent uncertainty within 20% [10], [11].

Given that materials and components of the nuclear power plants operate at elevated temperature (typical temperature for the structural materials and pressurized components is around 300°C), the derivation of the mechanical properties at the operational temperature is needed. The application of the nanoindentation at elevated temperature requires special equipment to avoid oxidation of the samples as well as to minimize drifts and ensure temperature stability on the indenter-sample contact. Some recent studies are referred for further reading, where the examples of high temperature nanoindentation are provided [12-18].

Given the physical nature of the indentation process, such an inverse FEA should preferably be based on a crystal plasticity model. Crystal plasticity FEM (CPFEM) nanoindentation research has been a hot topic over the last decade, from very general to particular ones. Beside the common parametrizations of material laws to analyze a material's response on nanoindentation, this technique can be used to study indentation size effects [19], pile-up formations [20][21], crystal orientations effects [22] or grain boundaries effects [23][24]. There are some research done on the use of CPFEM to simulate nanoindentation of metals for nuclear applications. Xiao and Terentyev used CPFEM to establish constitutive laws and simulate the nanoindentation response of tungsten as plasma-facing material in fusion reactors in reference and plasma-exposed states [25][26]. Nie and Lin demonstrated an excellent agreement between CPFEM and experimentally obtained *F-d* force-displacement and σ-ε stress-strain curves [27] and studied the irradiation impact on hardness [28] of ion-irradiated A508-3 BCC steel used for Reactor Pressure Vessel (RPV) construction.

The objective of this work is to apply a CPmodel in combination with FEM solver to simulate the process of nanoindentation in BCC iron as the model system of FeCr alloys and F/M steels, in order to establish the material law for further implementation and study of the contribution coming from the irradiation defects (such as dislocation loops and voids) to the plastic slip. The approach of using BCC Fe as a surrogate of the materials with more complicated microstructure is widely applied for multiscale modelling and related experimental campaigns within European projects (e.g. PERFECT [29], GETMAT [30] or M4F [31])The emphasis is put on the crystal plasticity theory because this would allow to correctly reflect the dislocation-defects interaction which comes directly from the atomic-scale studies [32]. Given that the mechanical properties of the nuclear structural materials need to be obtained at elevated temperature, the CPFEM model should include thermally activated and strain rate depended

equations to describe the plastic slip. While applying the CPFEM to polycrystalline materials, it is also important to have some means of validation to make sure that the modelled stress-strain states correspond to those that could be measured in real experiments i.e. compare the imprints of indents, compare the extension of the plastic strain around indents, and if possible compare the dislocation density profile around the indents. To minimize the ambiguity, we derive the constitutive laws using tensile deformation data. Then, the model accounts for thermal activation and strain rate (by considering the available theoretical and experimental data for the activation of dislocations in iron) and is fine-tuned when applied to reproduce the nanoindentation response. Importantly, the same material (batch of technically pure iron) is used throughout this study cycle to perform tensile tests, nanoindentation tests and microstructural examination to feed CPFEM with initial dislocation density and grain size. After the nanoindentation, the dimensions of the imprints as well as values of dislocation density around the indents are measured by means of scanning and transmission electron microscopy so as to offer one-to-one comparison with the predictions of the CPFEM. Altogether, the CPFEM model is prepared to include the presence of the irradiation defects via the modification of the dislocation slip rate parameters within the developed mathematical functional.

The work includes the description of the CPFEM model, tensile tests applied to derive the constitutive law, experimental nanoindentation study and subsequent microscopic analysis underneath indent and application of the FEM to simulate the nanoindentation process using tensile-derived data as main input source. The experiments and model validation is performed at room temperature and elevated temperature reaching up to 500°C.

2. Materials and methods:

2.1. Material

The technically pure iron was produced by OCAS (Gent, Belgium) using an induction furnace with vacuum chamber. A piece of the produced material was introduced into a pre-heated furnace to 1200°C for 1h and then hot rolled without interruption. The final stage was air-cooling to room temperature. The approximate eventual dimensions of the sheet were 10 x 250 x 600 mm^3.

To determine the chemical composition, two types of spectroscopies were used: spark source optical emission spectroscopy (SS-OES) to quantify all elements except Ni, Si, Al, and inductively coupled plasma optical emission spectroscopy (ICP-OES) to estimate Ni, Si, Al concentrations. The nominal chemical composition is presented is shown in Table 1:

Cr	**Ni**	**P**	**Al**	**Si**	**V**	**W**	**Cu**
0.002	0.007	0.003	0.023	0.001	< 0.0109	< 0.0099	< 0.0091
Mo	**Co**	**C**	**Nb**	**Ti**	**As**	**Sn**	
< 0.0082	< 0.0080	< 0.0067	< 0.0036	< 0.0020	< 0.0012	< 0.0010	

Table 1. Chemical composition of Fe in wt.%.

2.2 Tensile tests

The iron sheet described above was used to cut miniaturized dogbone specimens with dimensions of 1.5 x 4.2 x 16 mm^3 (5.2 mm gauge length) to perform uniaxial tensile deformation. The mechanical straining was done using Instron electro-mechanical universal test machine equipped with heating chamber and calibrated in accordance to Belgian accreditation rules (BELAC). Elongation of the sample was measured by the pull rod displacement and force by a load cell with 50 kN maximum capacity. The crosshead displacement rate was 0.02 mm/min in order to establish the strain rate of $6.6 \cdot 10^{-5}\ s^{-1}$ to coincide with the previously performed tests of the studied material on larger samples [33]. Due to the presence of C impurities in a concentration of 313 ppm (0.0067 wt.%), the material exhibits a significant dynamic strain ageing effect, thus the testing temperatures were chosen

where the impact of this phenomenon should be minimal or absent. Therefore, tests were done at room temperature, 400 °C and 500 °C.

2.3 Nanoindentation testing

As well as for dogbone specimens, the pure iron sheet described previously was used to cut 10 x 10 x 1 mm^3 specimen for nanoindentation testing. The surface preparation sequence consisted of the following steps: SiC abrasive grinding paper with 1200 grit → 2000 grit → 4000 grit, then diamond polishing paste with 3 µm → 1 µm particles diameter, and final polishing with colloidal silica suspension (OP-U). Each polishing stage lasted for at least 5 min.

The nanoindentation experiments were performed using a High Temperature nano-mechanical testing system from Bruker – the HYSITRON TI980 equipped with an xSOL 800 heating stage. The high temperature NI was carried out under a gas atmosphere (N_2 95at%; H_2 5at%) using a diamond indenter tip mounted by high temperature ceramic glue on a glass shank with low thermal expansion and low thermal conductivity. The xSOL stage allows for a tight temperature control of both – specimen and indenter tip in a small microenvironment, the 3D drawing of the stage is given in Figure 1.

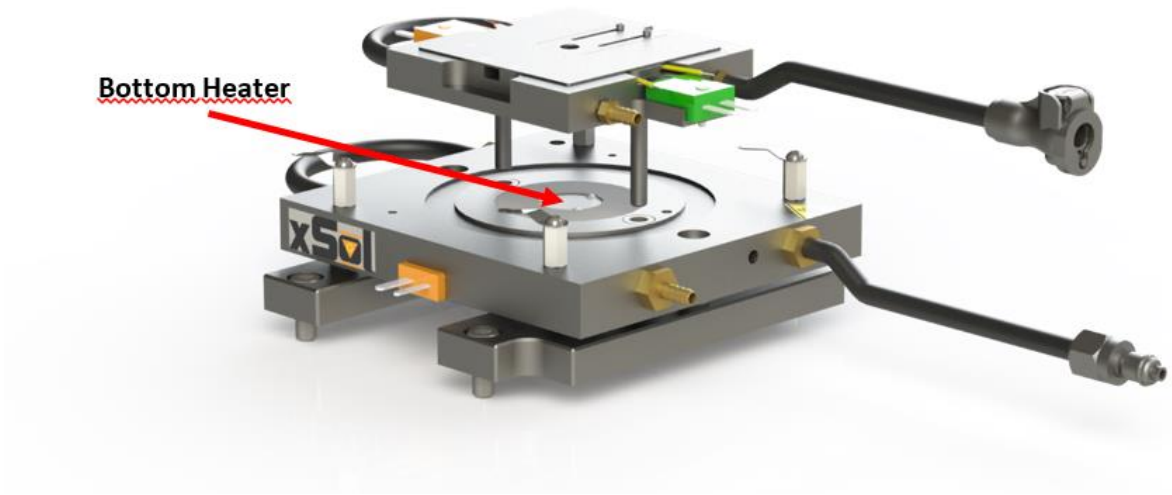

Figure 1. The schematic 3D drawing of the xSOL heating stage. The sample is placed on the bottom heater.

The specimen and indenter tip were located inside the xSOL heating stage that establishes a uniform temperature zone, heated by two ceramic heaters (below and above the microenvironment). The heaters are embedded in thermally isolating ceramic foam and encapsulated by a water cooled copper block and copper cover that isolates the heated zone and helps to maintain the test temperature of the instrument. A gasket seals the microenvironment in the xSOL stage. The gas environment in the xSOL stage was controlled by a constant inflow of gas that exits the stage through the hole in the top cover which enables optical observation of the sample with the light microscope and thereby also provides an access for the indenter tip. Fourmier gas (N_2 95at%; H_2 5at%) was chosen in the present study to protect the diamond tip and to reduce oxidation of the iron sample. However, for a full prevention of the oxidation at the highest temperatures of 400-500°C, a 20 nm SiO_2 layer was applied on the sample's surface. The sample mounting does not involve any embedding or gluing and was realized by mechanical clamping. After the temperature equilibration was performed, a set of single cycle NI was carried out in the force control mode up to 250 mN of maximum load, F_{max}. Six to nine standard measurements were performed for each condition using loading and unloading times of 5 s, applying a dwell time of 2 s and spacing between indents of 50 µm. The test temperature has an absolute error of about 1 K determined by the typical accuracy of thermocouples, while the relative error on the temperature is as good as 0.01 K. Given that passive indenter heating was applied here, the thermal drift may

increase during the penetration of the indenter (cold finger effect) due to the heat evacuation via the indenter rod. The compensation for such temperature drift was realized by heating of the indenter tip by the flowing gas. The sample and the tip were both located in a small chamber heated from the top and the bottom. The tip was heated by the gas inside the chamber and the radiation from the heaters around the chamber. Moreover, the tip was mounted on a thermally isolated shank. The sample and the tip were therefore at nearly the same temperature even for thermally non-conductive materials. The proof of the protection of the indentation area from the oxidation is provided in Figure 2 as a comparison of two iron specimens' surfaces with and without the application of SiO_2 layer after testing at 500°C, made with optical microscope.

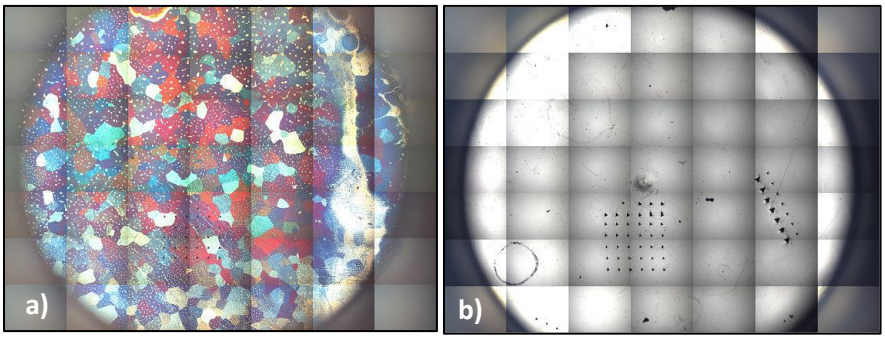

Figure 2. The surfaces of iron tested at 500°C: a) without, b) with the protective SiO_2 layer.

The indentation hardness values were determined using the classical Oliver & Pharr method [34] and fitting a power law to the first segment of the unloading curve (from 95% to 20%). The tip area function and the frame compliance were calibrated on fused quartz as described by the ISO14577 standard procedure.

2.3.1 Sample Coating Deposition

The formation of a Fe_xO_y-scale on the metal surface at elevated temperatures due to remaining oxygen in the xSOL chamber at temperatues of 500°C and higher, was prevented by a controlled coating with a thin film of amorphous silicon dioxide. This 20 nm thin layer acts as a hermetic oxygen barrier with negligible mechanical influence on the indentation tests in the microscale. The coating was applied with a Plasma Enhanced Chemical Vapor Deposition (PECVD) process using an *Oxford Plasmalab 80 Plus*. In contrast to classical CVD processes the PECVD allows coating at lower temperatures, which minimizes the influence on the sample microstructure. A process temperature of 300°C was used with a pressure of 1000 mTorr. The process gas flow rates were set to 170 sccm 5% SiH_4/95% N_2 and 710 sccm N_2O with RF-Power of 20 W @ 13.56 MHz. The film thickness was controlled by the process time and a growth rate that was previously determined for a sample with thicker SiO2 coating.

2.3.2 Fe_xO_y-scale formation vs. Controlled Deposition of SiO_2

The use of a protective coating layer to prevent oxidation is certainly not a new concept, although it is very seldom used during mechanical testing [35]. Here, a 20nm thin, silicon dioxide coating is used as that protective coating. However, it protects not just the underlying metal, but also to a certain extent protects the diamond probe from reacting with that same metal by reducing the available area and time of contact. There are several considerations to make here, primarily the relative effect of the protective film on the mechanical properties of interest. In the inverse case, measuring the properties of a thin film, the Buckle rule states that the indentation contact depth shall be 10% of the film thickness. In this case, measurements were made at 200x, or 20000% of the film thickness. The film may provide some minimal constraint to the pile-up and does show pop-in at fracture. However, the protective film prevents oxidation, even after hours at temperature. This, despite that both Ni and Fe rapidly oxidize, with neither forming a preventative barrier to further oxidation.

The xSOL system with Fourmier gas (95%N_2 mixed with 5%H_2 for a reducing atmosphere) has a residual O_2 concentration of roughly 80ppm, measured with the probe inserted and a 2 mm thick sample. This can be compared to the concentration of oxygen in a high performance glovebox, typically less than 1ppm, or to a vacuum system. For

comparison, we can compare the partial pressure of the gas to that of sea level air. So, with no control, that would be 0.21atm, or 21.3 kPa pO_2. In the xSOL, this gives an oxygen pressure of only 8 Pa pO_2. In the glovebox, operated at 1 atm, the oxygen partial pressure would be less than 0.1 Pa pO_2. Typically, gloveboxes are operated in a slightly positive pressure, so above 1 atm but for a simple calculation this is sufficient. We can compare this to the oxygen partial pressure found in an SEM, roughly 6.6 x 10^{-3} Pa, which is 0.0014 Pa pO_2.
This would suggest to try overcoming the difficulties by installing a nanoindenter inside a UHV-chamber that can be baked out, with an associated increase in effort and expense. However, even under UHV-conditions oxides layers start to form within seconds at 10^{-5} Pa with a rough change in rate of formation that would increase to tens of seconds with a corresponding decrease in vacuum level to 10^{-6} Pa, 100's of seconds at 10^{-7}, and so on. It has been found that these very low-pressure vacuum environments can only slow down the formation but cannot prevented it. To look at this in more quantitative terms of oxide growth rates is no simple task, although there is extensive work on simple alpha Fe in the literature. Iron has three primary valence oxides, wüstite (FeO) magnetite (Fe_3O_4) and hematite (Fe_2O_3), although wüstite is not stable below 570°C. Temperature and partial pressure both have strong roles in determining both the valence and the rate of growth. For example, at 400°C, above 1 Pa pO_2, hematite forms a protective layer to prevent magnetite growth, but at 0.1 Pa pO_2, the lack of oxygen prevents the creation of this protective film and causes increasing oxide thicknesses after 3 hours [36]. The temperature dependence of the oxidation rate is slightly more straightforward. In the parabolic growth regime, increases roughly one order of magnitude over each 100°C rise in temperature, from 1 x 10^{-11} $g^2cm^{-4}s^{-1}$ at 500°C [37]. The role of oxygen partial pressure appears to be much less than the role played by temperature. The use of a protective film of only 20nm is an easy way to circumnavigate the difficulty in preventing oxidation of Fe at high temperature.

It is also important to determine the stability of the protective layer. A simple Ellingham diagram can give insight into the equilibrium state of the system [38]. For temperatures from 0K to 1700K, the SiO_2 system has a significantly more negative Gibb's free energy of formation than for any of the oxides for Fe or Ni. Since the SiO_2 system was pregrown, the kinetics of formation are not really a concern.

2.4 Microstructural characterization

In order to correlate the results of the model with the change in microstructure a visual inspection of the area affected by the nanoindentation was performed using both scanning electron microscopy and transmission electron microscopy. The samples were prepared by focused ion beam milling (FIB) using a ThermoFisher Scios FIB/SEM instrument. First one of the indents created by the nanoindentation was selected. The area of interest was covered with a Pt layer to protect it from the ions. Care was taken to place the Pt layer over the deepest point of the indent. In this way the area to be analyzed is located near the tip of the indent, where the most severe damage is expected. Then, the lamella was cut free, lifted out from the sample and attached to a copper half grid. There, the lamella was thinned, below 200 nm. During the thinning, secondary electron and back-scattered electron images were recorded. The settings were optimized to get channeling contrast, which is related to the crystallographic orientation and can reveal the area of deformation. The TEM images were obtained on a JEOL 3010 TEM operating at 300 kV. Conventional bright field diffraction contrast TEM images, the corresponding diffraction patterns and convergent beam electron diffraction (CBED) patterns were recorded. The dislocation density was calculated at several locations for each specimen using the Digital Micrograph software and the average value was calculated. A circle was drawn in a random position of the TEM micrograph and the number of intersections of it with dislocation lines were counted. Then the dislocation density was calculated as $\rho = 2N/Lt$, where N is the number of intersections, L is the circle circumference, t the local thickness of the specimen at the taken area of the image, which is determined from the CBED pattern. The dislocation densities are corrected for extinction conditions assuming that all line dislocations have Burgers vector a/2<111>.

2.5 CPFEM for the nanoindentation of pure iron

The computational analysis in the presented work was done by coupling a user-defined material law (UMAT subroutine) implementing crystal plasticity theory with a FEM solver. The solver is combined with the gmsh open source three-dimensional finite elementmesh generator with a built-in CAD engine [39]. The CM3 libraries FEM solver was developed in the Aerospace and Mechanical Engineering Department of Liege University in Belgium, whereas the crystal plasticity routine was developed by Delannay et al. [40][41].

2.5.1 Modelling of plastic deformation

Plastic deformation in metals occurs by activation and glide of dislocations as well as by grain boundary deformation at high temperature and/or high strains or by twinning at low temperature and fast deformation. Here we assume that plasticity is caused only by dislocation glide as this is the main mechanism relevant for the structural materials. The strain rate is then controlled by the rate at which dislocations are released from pinning points, which is thermally activated and driven by the applied stress. Thermal activation and obstacles overcome by dislocations are predicted by Arrhenius-type equiation [42][43], where the backward jumps frequency at low stresses are controlled by hyperbolic sine function [44]. The dislocation slip rate $\dot{\gamma}^{\alpha}$ in a slip system α may be expressed as a function of the shear stress τ_{α} in this slip system:

$$\dot{\gamma}^{\alpha} = \dot{\gamma}_0 \exp\left(-\frac{G_0 \mu b^3}{k_b T}\right) 2\sinh\left[\frac{G_0 \mu b^3}{k_b T}\left(1-\left(1-\left(\frac{\tau_{\alpha}-\tau_c}{\hat{\tau}}\right)^{p}\right)^{q}\right)\right] \tag{2.1}$$

In this expression, $2H_k = G_0 \mu b^3$ represents the value of kink-pair formation enthalpy for a screw dislocation, where $\mu = (C_{11} - C_{12} + 2C_{44})/4$ is the shear modulus, b is the magnitude of Burger's vector, and G_0 is a constant. $\dot{\gamma}_0$ is a reference slip rate, $k_b T$ is the product of Boltzmann constant and temperature, and p and q are constants describing the profile of Peierls potential barrier, being equal to 0.5 and 1.5 respectively [45]. Here we consider the critical resolved shear stress at 0 K as a sum of an athermal stress τ_c, natural for BCC metals, and the maximum value of the thermal stress $\hat{\tau}$.
The athermal stress may be expressed as a function of the dislocation density as follows:

$$\tau_c = S_0 + h_{dis} \mu b \sqrt{\rho} \tag{2.2}$$

where h_{dis} is the dislocation strength coefficient and S_0 accounts for the contribution of the lattice friction stress and the Hall-Petch effect [46]. ρ is the dislocation density which evolves according tothe modified law proposed by Kocks and Mecking [47], where k_2 is computed from the saturated dislocation density value ρ_{sat} and remains constant, and the temperature and strain rate effects are controlled by the term ξ [48]:

$$\dot{\rho} = \left(k_1 \sqrt{\rho} - k_2 \xi \rho\right) \dot{\Gamma} \tag{2.3}$$

$$\rho_{sat} = \left(\frac{k_1}{k_2}\right)^2 \tag{2.4}$$

$$\xi = \left\{1 - \left(\frac{k_b T}{G_0} ln \frac{\dot{\gamma}_0}{\dot{\Gamma}}\right)^{1/q}\right\}^{-1/p} \tag{2.5}$$

where $\dot{\Gamma}$ is the sum of slip rates in all of the slip systems:

$$\dot{\Gamma} \triangleq \sum_{\alpha} |\dot{\gamma}_{\alpha}| \tag{2.6}$$

2.5.2 Mathematical formulation of crystal plasticity

Under finite strains, the mapping from the undeformed (reference) configuration $\mathbf{x}$ into the deformed (current) configuration $\mathbf{y}$ is described by the second-rank deformation gradient tensor $\mathbf{F}$. The derivation of the model equations was inspired by a number of works on crystal plasticity [49-52]. As commonly assumed in crystal plasticity theories, the deformation gradient is multiplicatively decomposed in: $\mathbf{F} = \mathbf{R}^{*}\mathbf{F}^{el}\mathbf{F}^{p}$, where $\mathbf{R}^{*}$ represents the lattice rotation, $\mathbf{F}^{el} = \mathbf{I} + \boldsymbol{\varepsilon}^{el}$ is the elastic strain, (which is infinitesimal in metals, $\|\boldsymbol{\varepsilon}^{el}\| \ll 1$), and $\mathbf{F}^{p}$ – is the deformation

caused by dislocation slip. A spatial gradient $\mathbf{L}$ which quantifies the relative velocity between two positions of the current configuration is called velocity gradient and given by:

$$\mathbf{L} = \nabla \mathbf{v} \tag{2.7}$$

where $\mathbf{v}$ is a nonzero velocity field which stands for a time-dependent displacement $\mathbf{u} = \mathbf{y} - \mathbf{x}$ and given by the time derivative of the corresponding displacement field:

$$\mathbf{v} = \frac{\mathrm{d}\mathbf{u}}{\mathrm{d}t} = \dot{\mathbf{u}} = \dot{\mathbf{y}} \tag{2.8}$$

The relation of the velocity gradient and the deformation rate $\dot{\mathbf{F}}$ can be derived from the equivalence of the relative change in the velocity of two points separated by $d\mathbf{y}$ and the deformation rate of their relative position:

$$\mathbf{L}d\mathbf{y} = \frac{\partial \mathbf{v}}{\partial \mathbf{y}} d\mathbf{y} \equiv \frac{d}{dt} d\mathbf{y} = \frac{d}{dt} \mathbf{F} d\mathbf{x} = \dot{\mathbf{F}} d\mathbf{x} = \dot{\mathbf{F}}\mathbf{F}^{-1} d\mathbf{y} \tag{2.9}$$

then, comparing the left-hand and right-hand sides of Eq. (2.8), the velocity gradient tensor $\mathbf{L}$ can be expressed as:

$$\mathbf{L} = \dot{\mathbf{F}}\mathbf{F}^{-1} \cong \mathbf{R}^{*} \left[\dot{\tilde{\boldsymbol{\Omega}}}^{*} + \dot{\tilde{\boldsymbol{\varepsilon}}}^{\boldsymbol{el}} + \underbrace{\sum_{\alpha} (\mathbf{b}^{\alpha} \otimes \mathbf{m}^{\alpha}) \dot{\gamma}^{\alpha}}_{\tilde{\mathbf{L}}^{p}} \right] \mathbf{R}^{*^{T}} \tag{2.10}$$

where $\mathbf{L}^{p}$ is the plastic velocity gradient, $\dot{\tilde{\boldsymbol{\Omega}}}^{*} = \mathbf{R}^{*^{T}} \dot{\mathbf{R}}^{*}$ is the lattice spin (i.e. rate of crystal rotation), $\mathbf{b}^{\alpha}$ and $\mathbf{m}^{\alpha}$ are unit vectors along the Burger's vector and normal to the α^{th} slip plane. The dislocation slip rate $\dot{\gamma}^{\alpha}$ in the slip system α is calculated by Eq. (2.1). The anisotropic elastic stiffness operator $\mathbf{C}$ is used to compute the Cauchy stress tensor $\tilde{\boldsymbol{\sigma}} = \mathbf{C} : \tilde{\boldsymbol{\varepsilon}}^{el}$, which is expressed in coordinates that rotate together with the crystal frame (corotational tensor). The plastic velocity gradient $\mathbf{L}^{p}$ can be rewritten as:

$$\tilde{\mathbf{L}}^{p} = \sum_{\alpha} \tilde{\mathbf{M}}^{\alpha} \dot{\gamma}_{\alpha} = \sum_{\alpha} (\tilde{\mathbf{M}}^{\alpha}_{sym} + \tilde{\mathbf{M}}^{\alpha}_{skw}) \dot{\gamma}_{\alpha} \tag{2.11}$$

where $\tilde{\mathbf{M}}^{\alpha}$ is the Schmid tensor subdivided into a symmetric $\tilde{\mathbf{M}}^{\alpha}_{sym}$ and a skew-symmetric $\tilde{\mathbf{M}}^{\alpha}_{skw}$ part. The material response is calculated incrementally by time integration using a Newton-Raphson scheme under an above-mentioned velocity gradient expressed as $\mathbf{L} = \mathbf{D} + \mathbf{W}$, where $\mathbf{D}$ and $\mathbf{W}$ are symmetric and skew-symmetric strain rate tensors respectively. The set of differential equations is built by separating symmetric and skew-symmetric tensors:

$$\begin{cases} \dot{\tilde{\boldsymbol{\sigma}}} = \mathbf{C} : (\mathbf{R}^{*^{\mathrm{T}}} \cdot \mathbf{D} \cdot \mathbf{R}^{*} - \sum_{\alpha} \tilde{\mathbf{M}}^{\alpha}_{sym} \dot{\gamma}_{\alpha}) \\ \dot{\tilde{\boldsymbol{\Omega}}}^{*} = \mathbf{R}^{*^{\mathrm{T}}} \cdot \mathbf{W} \cdot \mathbf{R}^{*} - \sum_{\alpha} \tilde{\mathbf{M}}^{\alpha}_{skw} \dot{\gamma}_{\alpha} \end{cases} \tag{2.12}$$

2.5.3 Standalone mode Taylor-type modelling

The CP model can be used either standalone or coupled with a finite element solver (CPFEM mode). In the standalone mode, the model equations are applied to a theoretical (virtual) polycrystal, in which every grain undergoes the same strain as the polycrystal as a whole (Taylor mean-field crystal plasticity model [53]). The grains of this virtual polycrystal cannot be defined in terms of their geometrical shape and size, and their arrangement cannot be prescribed. Thus, the effect of these factors on the mechanical response is disregarded. However, a specific crystallographic texture may be assigned to the polycrystal. Even though the iso-strain assumption makes the

approach less realistic than CPFEM, the standalone calculations rely on the same mathematical modelling of dislocation slip and allow us to capture the main macroscopic trends.

Here, the CP model was applied to a polycrystal with a random texture consisting of 1000 grains to fit the model equations to the results of uniaxial tensile tests of iron. The computational cell was stretched in direction x at a given temperature and strain rate, and was free to deform along directions y and z. The values of average true stress and strain in the polycrystal were recorded during the simulation and compared with the curves obtained experimentally. The model parameters were adjusted until a good match was reached between the experimental and the calculated curves. The obtained parameters were then used in CPFEM simulations of indentation.

2.5.4 FEM setup

A 100 x 100 x 50 μm^3 single crystal specimen box with perfect shape Berkovich indenter was used as nanoindentation FEM setup, see Figure 3.

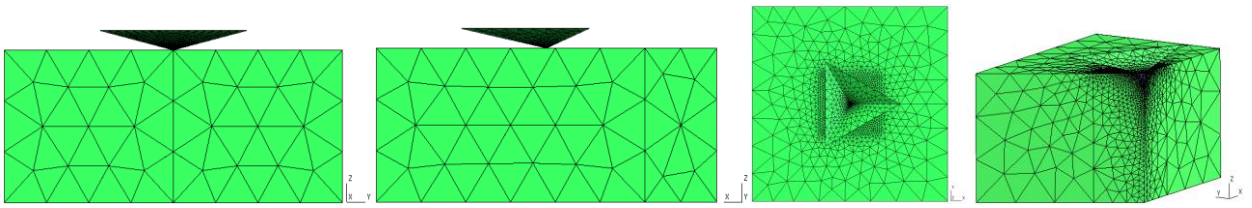

Figure 3. The geometry of nanoindentation FEM setup.

The bottom plane of the box was constrained by *x, y, z* axes and the side planes were constrained along their normal axis only, in order to avoid an expansion of the box in case if dimensions are too small for a particular indentation depth. The mesh was refined next to the tip with the smallest characteristic length of the element of 0.125 µm. Overall it had 7725 nodes and 36682 tetrahedral 1st order elements in which locking is avoided by averaging the volumetric deformation. The single crystal orientations were set for indenter's immersion successively along [100], [101] and [111] directions as the three ultimate cases of surface orientations. However, as will be shown further, the outcoming CPFEM nanoindentation force-displacement curves slightly change depending on the crystal orientation (≈3.5% as the most), so such choice of the directions is a tool to study the corresponding stress-strain fields created by the indenter tip.

3. Results

3.1 Experimental data

3.1.1 Stress-strain curves from tensile tests

The obtained tensile force-displacement curves were firstly recalculated into engineering stress-strain by using the standard formulas:

$$\sigma_{eng} = \frac{F}{A_0}, \varepsilon_{eng} = \frac{\Delta L}{L_0} \quad \textbf{(3.1)}$$

The obtained engineering stress-strain curves are presented on the Figure 4(a). Then the Young's modulus of the curves was corrected to the value of 210 GPa (to remove the machine compliance) by applying the following correction:

$$\varepsilon_{eng_{corr}} = \varepsilon_{eng} + \sigma_{eng}(\frac{1}{E} - \frac{1}{E_{exp}}) \quad \textbf{(3.2)}$$

where E = 210 GPa and E_{exp} is the Young's modulus calculated from the tensile tests (approx. 23 GPa due to the machine compliance). One could note a weak presence of the yield drop phenomenon on the curve from the room temperature test (Figure 4, a), so this part was subtracted. Afterwards, the engineering stress-strain curves were recalculated in true stress-strain relationships by using the standard formulas:

$$\varepsilon_{true} = \ln(1 + \varepsilon_{eng}), \sigma_{true} = \sigma_{eng}(1 + \varepsilon_{eng}) \quad \textbf{(3.3)}$$

and cut at 15% of strain. The obtained stress-strain curves are shown in Figure 4.

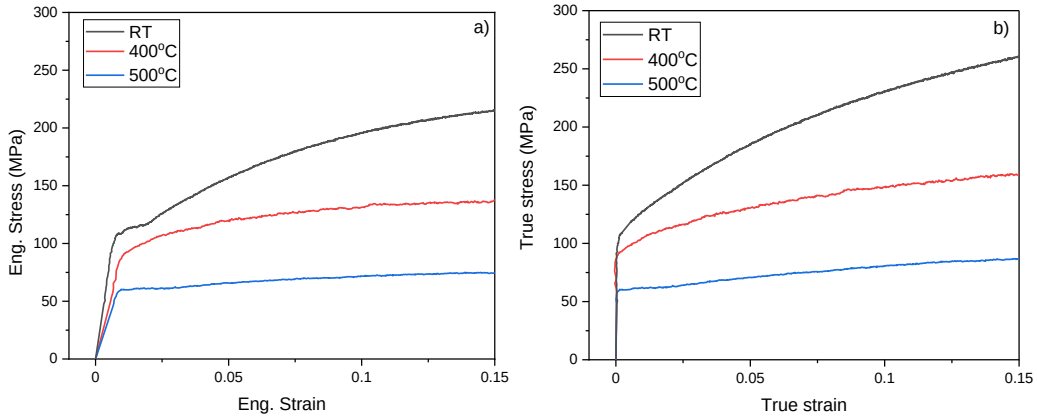

Figure 4. Engineering (a) and true (b) stress-strain tensile curves of iron with described corrections.

One can note that the yield stress at 400°C is closer to the value of the yield stress at room temperature, than to the one at 500°C. The reason for this is attributed to the previously discussed dynamic strain ageing effect, which is still affecting the onset of the dislocation glide at 400°C. This fact will be considered at the stage of determination of the constitutive parameters.

3.1.2 Force-displacement curves from nanoindentation tests

The force-displacement nanoindentation curves were obtained at room temperature, 400°C and 500°C and the averaged curves are presented in Figure 5. Since at least six tests were done for each temperature in the force-controlled mode, the summarized result has a scatter by displacement axis (due to different material resistance depending on a grain orientation), so the curves were averaged, where deviation is shown by X error bar. Thermal drift was measured for each single indentation and in average equals to 0.7±0.47 nm/s at the room temperature, -0.07±0.1 nm/s at 400°C and 0.27±0.17 nm/s at 500°C. As expected, the increase of temperature suppresses the material's resistance to plastic deformation, so the same force of 250 mN immerses the indenter up to ≈3 µm at room temperature, and up to ≈4 µm at 500°C. One can also note, that the hold at the maximum force shows an increase in the displacement with increase of temperature, which is the expected behavior due to the high temperature creep relaxation. This fact seems to affect nanoindentation pile-up behavior, as shown on Figure 6, where the overall pile-up height decreases with the temperature. Moreover, as it happens under tensile deformation, due to the present dynamic strain ageing effect at 400°C, the corresponding force-displacement curve appears closer to the room temperature one, rather than to 500°C.

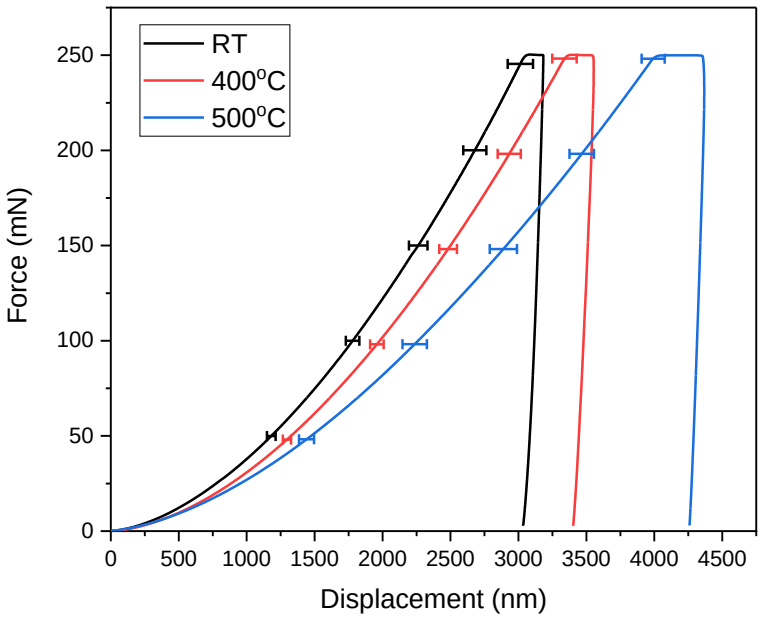

Figure 5. Averaged nanoindentation force-displacement curves.

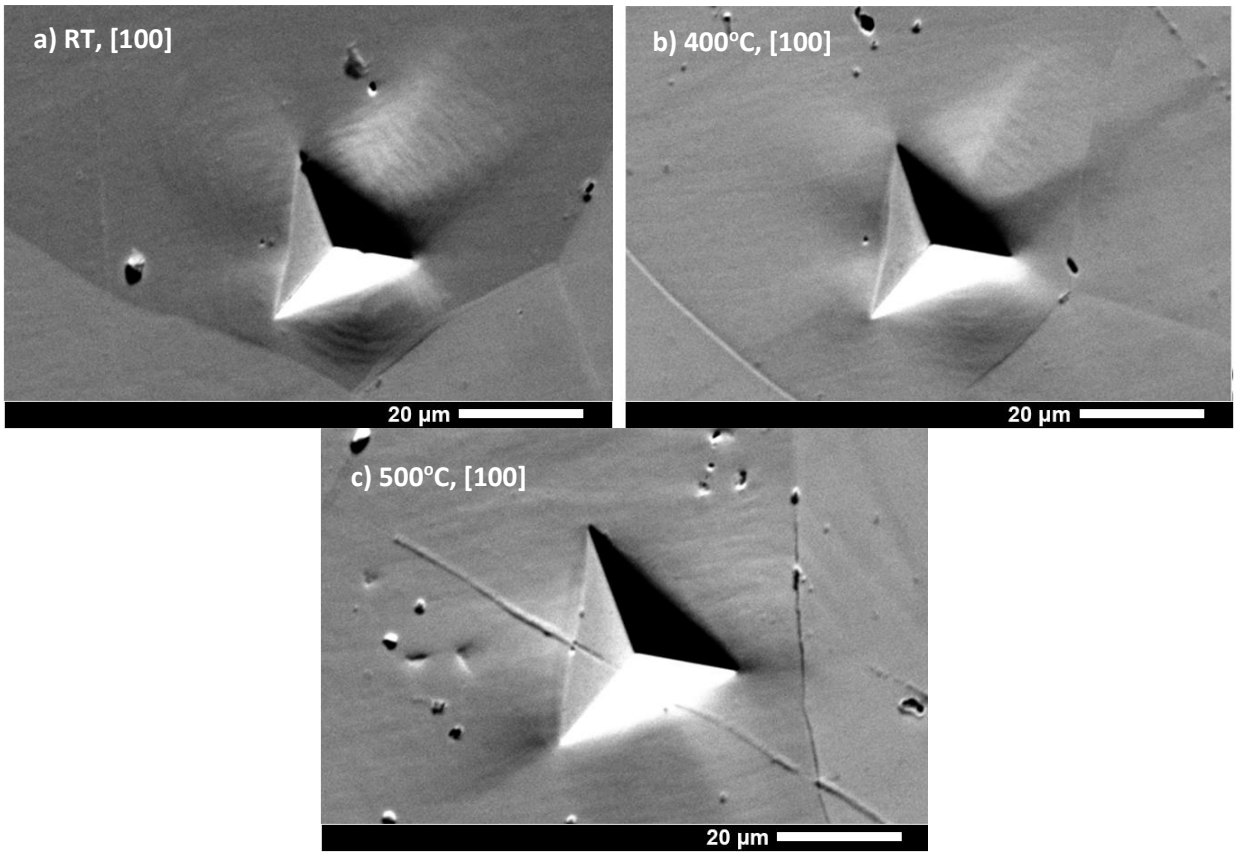

Figure 6. Nanoindents on [100] surface orientation obtained by SEM: a) at room temperature, b) at 400°C, c) at 500°C.

3.2 Microstructure analysis

The microstructural examination presented below was applied on the 1.5 µm depth indents performed at room temperature. The main purpose of that examination was the derivation of the microstructural characteristics which could be compared with the output of the modelling. The examination included the SEM analysis of the indents (in order to evaluate indentation pipe-up/sink-in microstructural profiles), the extraction of the lamellas underneath the indents with sub-sequent SEM and TEM analysis to estimate the extension of the plastic zone created by indenter tip, and to determine the dislocation density in several regions as it was described in paragraph 2.5. The extracted information was then used to reduce an uncertainty on the model parameters as well as to validate the accuracy of the model in terms of the plastic deformation features induced as a result of the nanoindentation**.**

3.2.1 SEM inspection of the sub-surface lamella

The sample of ≈10×10×0.2 µm was extracted from the indented surface and polished by FIB to produce the final lamella such as shown in Figure 7. The lamella was first inspected by SEM using backscattered electrons (BSE) (Figure 7(a)) and secondary electrons (SE) (Figure 7(b)) modes, and then inspected by TEM.

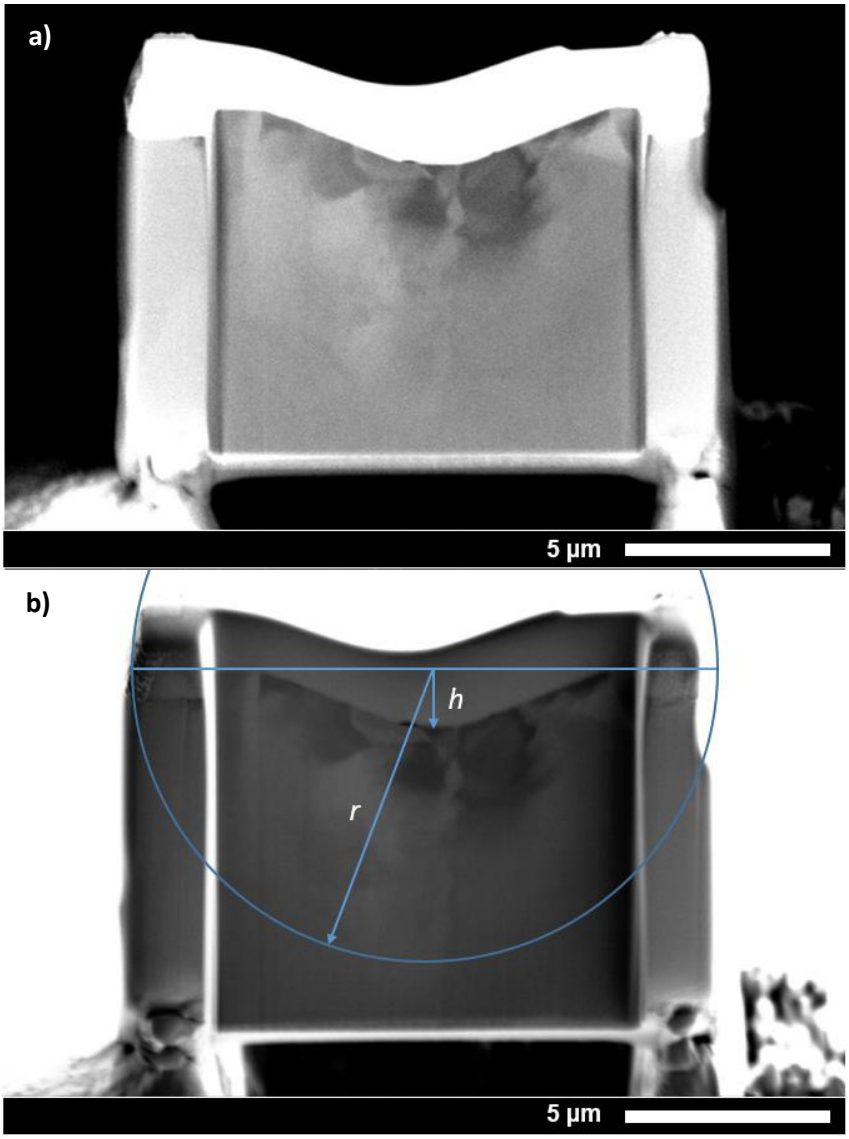

Figure 7. The lamella inspected with SEM taken from below the indent: a) BSE mode, b) SE mode with roughly estimated plastic zone radius.

The plastic deformation induced by the indentation process can be seen thanks to the contrast on BSE and SE images. While the indentation depth is well resolved thanks to the surface contour under platinum layer. By the rough estimation of the plastic zone hemisphere (see Figure 7(b)) we can calculate that the ratio of the indentation depth h = 1.5 µm to the plastic zone radius $r \approx 8$ µm is equal to 5.3, which is in expected range of 5-10 for metals as was reported earlier in Refs. [54], [55]. This information will then be compared with the analysis of the stress-strain fields under the indent as obtained by the CPFEM.

3.2.2 Dislocation density analysis by TEM

The second step in the microstructural analysis was characterization by TEM. The main objective was to characterize the pattern of the dislocation density and make an estimate of the variation of the dislocation density as function of distance from the indent tip.

The initial microstructure of the material (i.e. before the indentation) was studied previously in [33] by TEM in order to estimate the dislocation density in the non-deformed and pre-strained to 15% specimens. Eventually, the average dislocation density was calculated as 10^{12} m^{-2} for the non-deformed specimen and 2×10^{14} m^{-2} in the pre-strained to 15% state. This information will be used in our model to calibrate the constitutive model.

Also the lamellas taken from underneath of the indent and from a reference part of the specimen by the method described before were used for TEM investigations. Figure 8 and 9 show the dislocation structure underneath the indent.

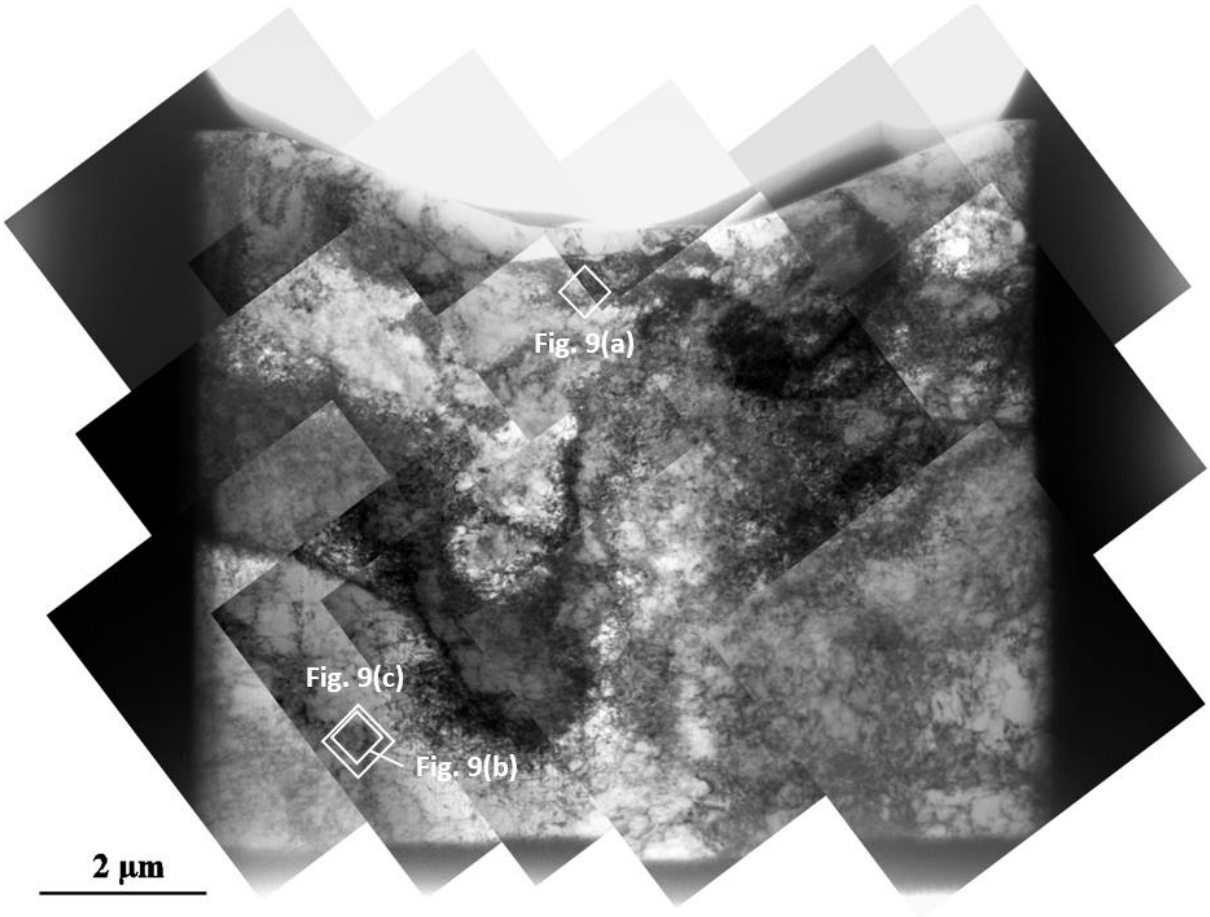

Figure 8. Composite picture of dislocation structure in the lamella, extracted from the region underneath the indent, inspected by TEM

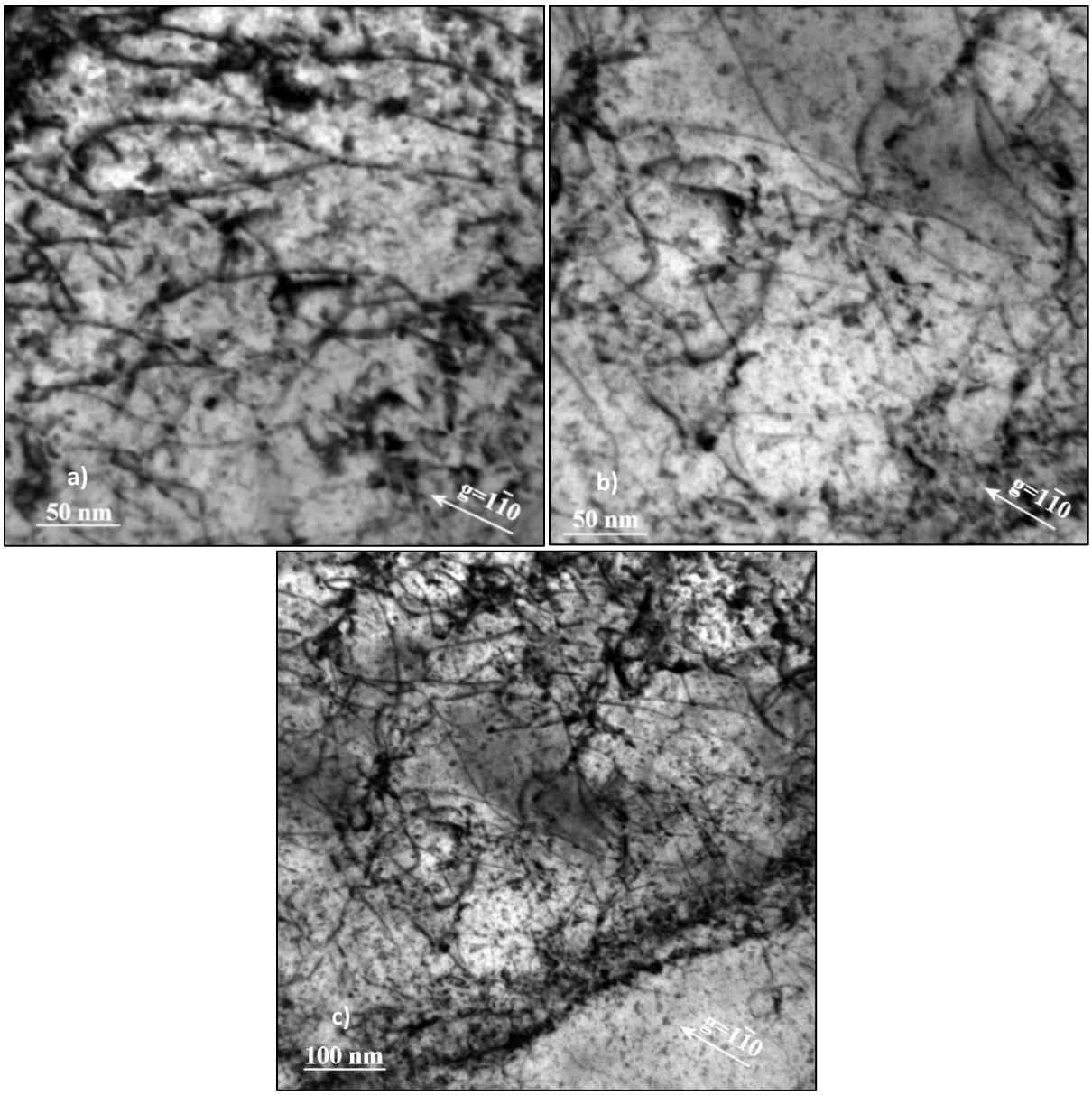

Figure 9. Dislocation structure in the specific places of the lamella inspected by TEM: a) dislocation structure near the tip, b) dislocation structure in the bottom of the lamella, c) dislocation slip band in the bottom area of the lamella.

The dislocation density was determined at three different locations in the lamella. In this way, the density of 1.37×10^{15} m^{-2} (Figure 9(a)) near the tip of the indent, 0.91×10^{15} m^{-2} (no micrograph provided) in the middle of the lamella, and 0.85×10^{15} m^{-2} (Figure 9(b)) in the bottom of the lamella were calculated. It should be noted that the precision of the individual measurements is very low and even though the value suggests a higher density near the tip of the indent, the difference may not be statistically significant. The average dislocation density below the indent were calculated as $(1.0\pm0.2)\times10^{15}$ m^{-2}.

In general, the dislocations are tangled and homogeneously distributed, however, there are some locations, for example in the bottom part of Figure 9(c), where the dislocations are starting to form dislocation bands. The observed defect structure suggests that the stress induced by the indentation creates a high amount of dislocations, which are moving away from the indent. The only obstacles for the dislocation glide are dislocations initially present

in the non-deformed bulk material and dislocations created by the indentation (no grain boundaries were found within the lamella). This results in a high density of tangled dislocations. When the movement of the dislocations is blocked, dislocations bands can be formed, which are oriented perpendicular to the movement of the dislocations. In this sample, several of such bands were observed to be oriented roughly parallel to the sample surface. It agrees with the common understanding of that the plastic deformation zone is created at and moves away from the indent. The observed dislocation bands propagate deeper into the material, than it can be observed from the lamella, so depth of the plastic deformation area is somewhat more than the size of the lamella and, therefore, larger than it was assumed just by using SEM contrast fields.

3.3 Adoption of constitutive laws

In order to establish the material elasto-plastic deformation law, a set of parameters had to be determined. The following information needed to be compiled. The number of slip systems used was 24, the elastic constants C_{11}, C_{12}, and C_{44} can be found here [56] (assumed to be constant for all of the studied temperatures), Burgers vector was taken for the $\frac{a}{2}\langle 111\rangle$ dislocation (so the magnitude of the Burgers vector is $\sqrt{3}\frac{a}{2}$), where a is the lattice parameter of 2.856 Å [57] (assumed to be constant for all of the studied temperatures) of α-Fe, initial and saturated dislocation densities were taken from the TEM measurements mentioned above, and the kink pair formation enthalpy was determined in Ref. [58]. However, the value used in the model was slightly modified to correctly reflect the presence of carbon impurities, which are expected to interact with the kinks thereby effectively increasing the apparent activation energy (atomistic simulations describing such interaction can be found here [59]). Other parameters had to be fitted in order to correctly reproduce the true stress-strain (*σ-ε)* curve.

Once the obtained set of parameters was established and validated, it had to be correctly transferred as an input for nanoindentation simulations, taking into account the difference in the Hall-Petch contributions. Given that the average grain size of 100 µm, even the most deep indent (4 µm depth) at 500°C having the maximal possible plastic zone radius of ≈40 um is not large enough for dislocation movement to be effectively "blocked" by a grain boundary, while dislocation-grain boundary interaction readily happens in the uniaxial tension of a polycrystalline sample. Therefore, the Hall-Petch stress contribution was neglected in the simulation of the nanoindentation, by reducing S_0 by 4 MPa, and this was found to provide a better agreement with experimental data (cfr. to the case of inclusion of the Hall-Petch contribution).

The summary of the parameters applied in the set of constitutive equations is provided in Table 2.

Parameter	Value for tensile curve	Source
Elastic coefficient, C_{11}	230 [GPa]	Literature [56]
Elastic coefficient, C_{12}	135 [GPa]	Literature [56]
Elastic coefficient, C_{44}	117 [GPa]	Literature [56]
Burgers vector, b	0.2482 [nm]	Literature [57]
Reference slip rate, $\dot{\gamma}_0$	10^3 [s^{-1}]	Fitted
Lattice friction stress + Hall-Petch stress, S_0	21-13 (17-9) [MPa]	Fitted
Initial dislocation density, ρ_0	10^{12} [m^{-2}]	Measured
Kink pair formation enthalpy, $2H_k$	2.365 [eV]	Literature [38]/Artificially increased [59]
Dislocations interaction strength, h_{dis}	0.21 – 0.07	Fitted
Saturated dislocation density, ρ_{sat}	$1.3\cdot10^{15}$ [m^{-2}]	Measured
Kocks-Mecking parameter, k_1	$1.3\cdot10^{8}$ [m^{-1}]	Fitted
Thermal stress, $\hat{\tau}$	47.0 [MPa]	Fitted

Table 2. The list of constitutive parameters used to simulate the constitutive law of iron.

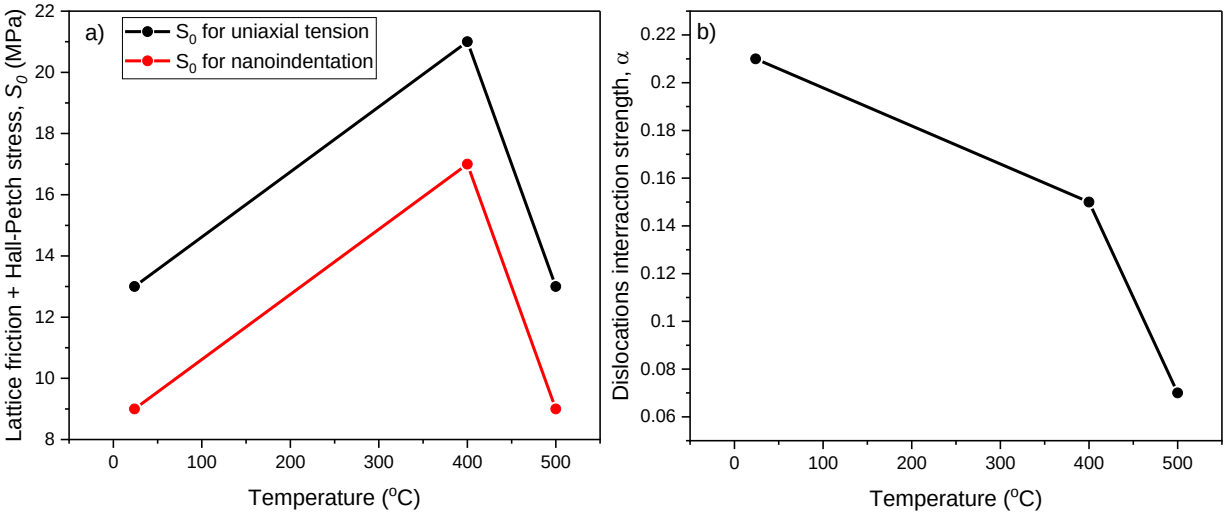

Figure 10. Lattice friction + Hall-Petch stress S_0 (a) and dislocations interaction strength h_{dis} (b) versus temperature.

As it was mentioned above, the carbon interstitials seem to be still contributing to the stress needed to start the dislocation movement at 400°C, so this fact was taken into account by increasing the S_0 value from 13 to 21 MPa (Figure 10(a)) for this temperature to simulate the uniaxial tension, and from 9 to 17 MPa (subtracting 4 MPa of the Hall-Petch effect) for the nanoindentation simulation, whereas room temperature and 500°C values are equal to each other. The S_0 remains constant, despite the inverse dependence of the friction stress of temperature, because the thermal stress $\hat{\tau}$ value presented in (2.1) is responsible for the thermal effects in the applied model. Since the still present carbon interstitial clustering at 400°C affects the expected gradual yield stress decrease, the S_0 was artificially increased in order to account to this effect. The dislocation-dislocation interaction coefficient (see Figure 10(b)) decreases with the increase of temperature, which is the expected trend for BCC metals [52].

The constitutive parameters presented in Table 2 are correspondingly used to perform the simulations of uniaxial tension applied to a polycrystalline sample consisting of 1000 grains. The σ-ε curves obtained from those simulations carried at RT, 400 and 500°C are presented in Figure 11(a). To demonstrate the quality of the obtained match, the ratio of the simulated curve to the experimental one was expressed in percent and plotted versus true strain starting from ε_{true} = 0.2% in Figure 11(b). As it can be seen, the maximum difference between the pair of experimental and simulated curves at room temperature stays within 2%, reaches 5% for 400°C and does not exceed 7% at 500°C. The yield stress values agree with experimental data within 2% of divergence.

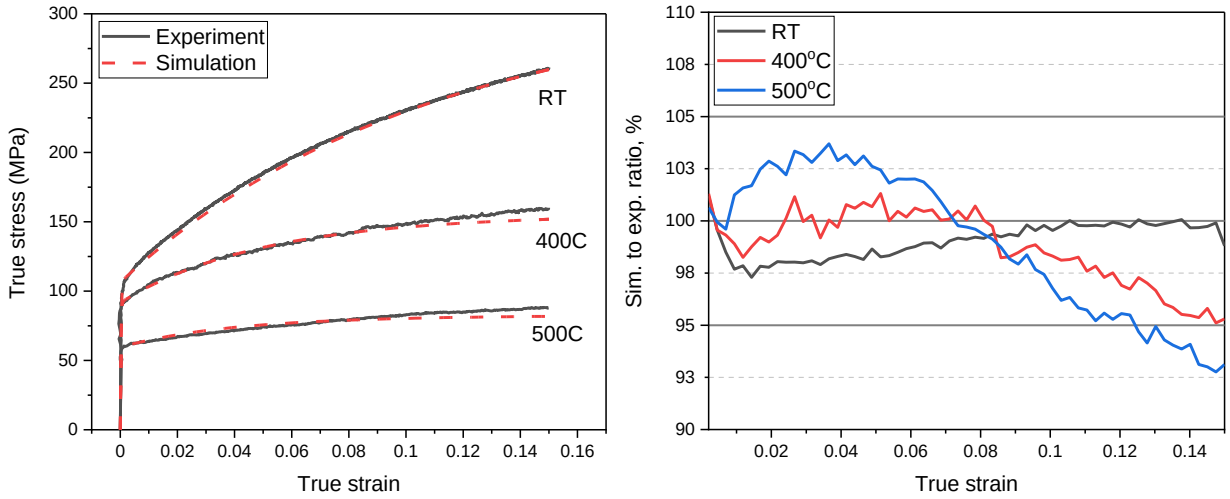

Figure 11. a) Simulated (dashed red) and experimental (solid black) true stress-strain curves of iron in comparison, b) simulation to experimental σ-ε curves ratios in percent.

As the CPFEM simulations were performed, the dislocation density as a function of attained strain was reported, see Figure 12. As one can see, the development of the dislocation density is found to be in a good agreement with the TEM measurements done at the elongation corresponding to 15% of true strain [33], see Section 3.2.

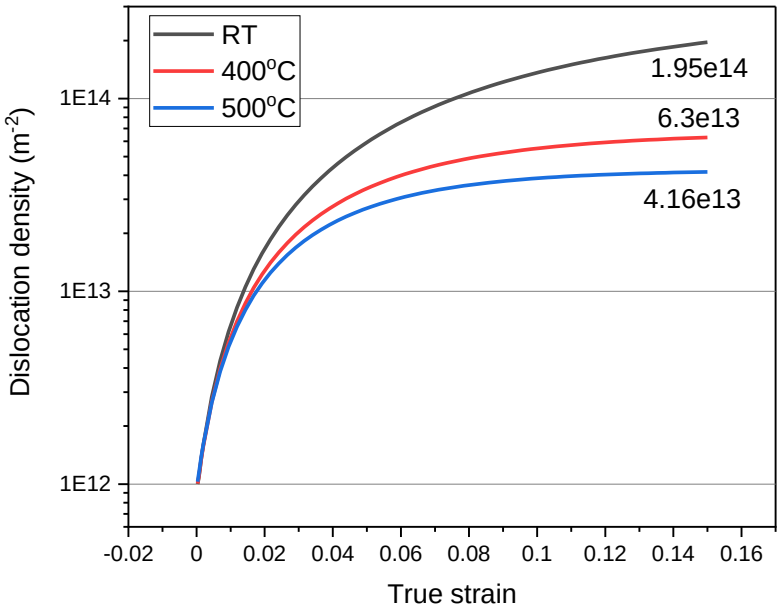

Figure 12. Dislocation density (log scale) vs. true strain for the three temperatures.

3.4 Nanoindentation simulations

By applying above described FEM setup and constitutive laws, the nanoindentation tests were simulated at RT, 400°C and 500°C. The resulting force-displacement curves were obtained with respect to the three crystal orientations, and then averaged to provide a comparison with the experimental ones, as presented in Figure 13. Figure 13(d) contains the separated force-displacement curves for each of the three orientations. It is clearly seen that in case of the indenter immersion along [100] direction, material shows a slightly lower resistance to the deformation (≈3.5% difference between [100] and [111] at RT).

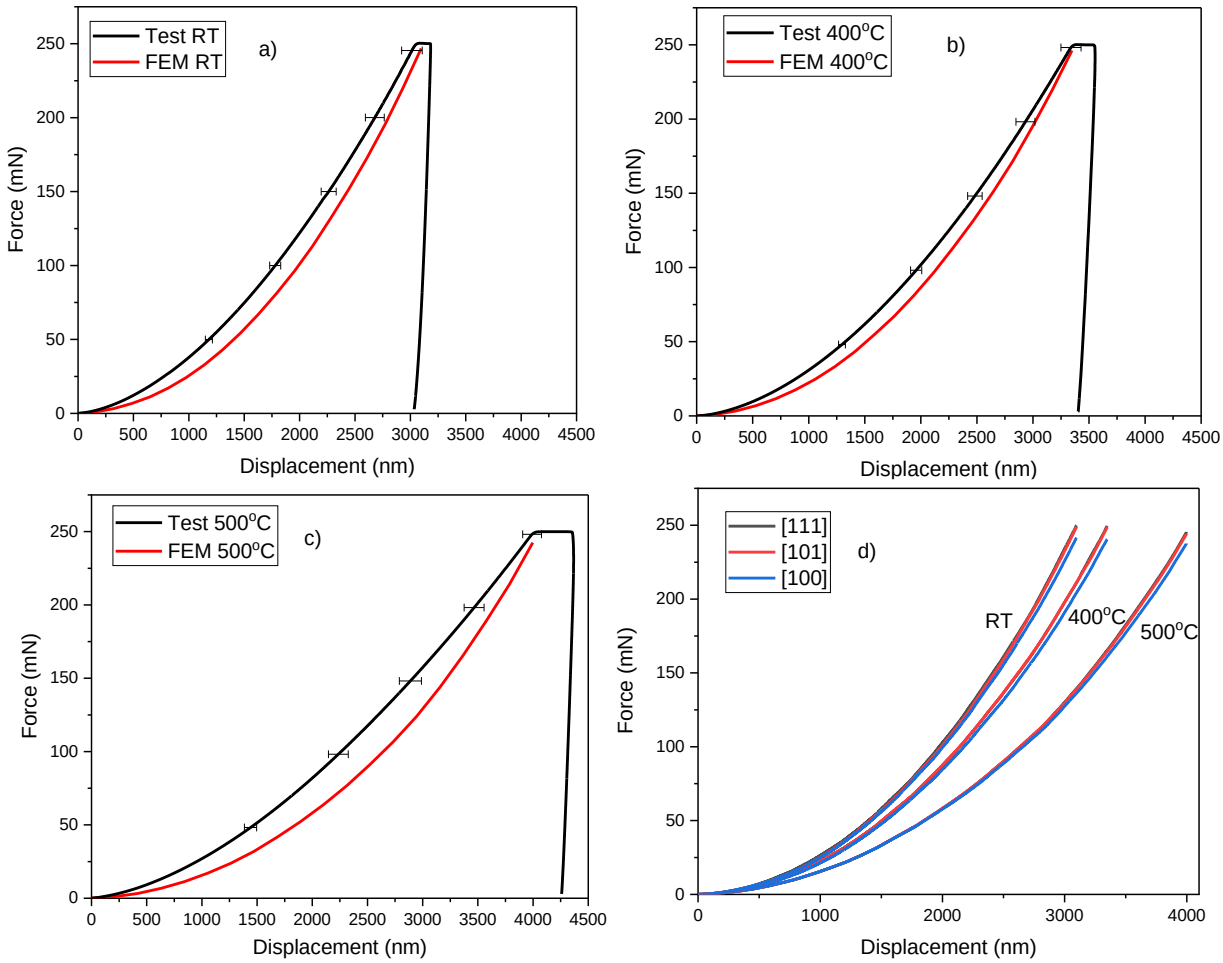

Figure 13. Averaged nanoindentation force-displacement curves obtained from experiment (black) and FEA (red) in comparison: a) room temperature, b) 400°C, c) 500°C; d) Single curves by grain orientation.

The output force at h_{max} matches well with the experimental data, however, the CPFEM curves are strongly underestimating the experimental ones on the shallow depths (up to 60% difference at 250-500 nm) which consequently affects the further force evolution. To improve this, the strain gradient theory [60] must be implemented into the CPFEM setup, which however implies a cumbersome and dedicated implementation and computational effort. Another reasons for the observed difference between the curves can come from the experimental artifacts, such as limited surface roughness, machine compliances, thermal drifts, uncertainties on the low depths, etc.

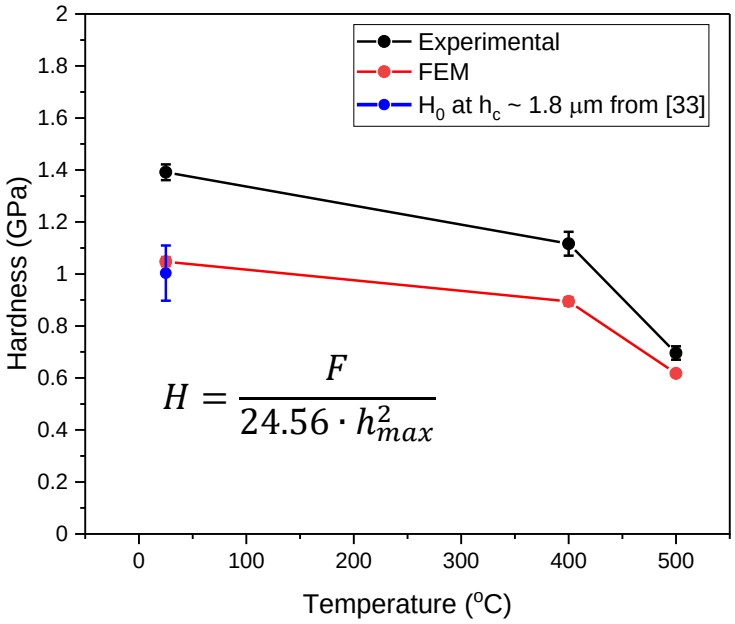

Figure 14. Hardness values calculated from experiment (black), FEA (red) and taken from [33] (blue) in comparison.

Given the simulated load-displacement curves and the patter of the indents, the hardness was calculated using FEM data and compared to the experimentally measured values, see Figure 14. One can see that the hardness values from the CPFEM coincide well with the hardness values of the same material taken from [33] where the elastic modulus correction (EMC) procedure was applied. However, in this study the contact depth h_c for CPFEM curves was not calculated using the unloading stiffness S at P_{max}, as proposed in the Oliver and Pharr method [34], and just taken equal to h_{max}. Hence, the contact area is calculated as $A = 24.56^2 \cdot h_{max}$ which is fair for a perfectly sharp indenter and which is our case in this simulation. Hence, we can see that the general trend for the hardness predicted by the simulations is correctly reproduced, but the absolute value is underestimated by the CPFEM. This underestimation may be, at least partially, explained by the need to apply EMC procedure to the experimental data. However, the high temperature measurements were performed before the results of Ref. [33] were published.

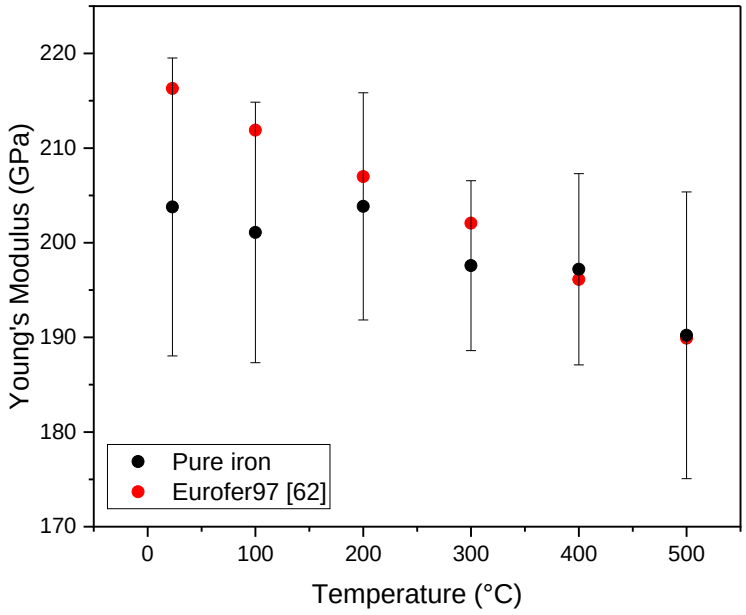

Figure 15. Young's modulus values obtained from nanoindentation experiments for pure iron (black) and by E111-04 ASTM standard [61] for Eurofer97 [62] (red) in comparison.

On Fig. 15 we compare the young's modulus values obtained from nanoindentation experiments for pure iron and by using E111-04 ASTM standard for Eurofer97 steel. Both materials correlate well and follow the expected trend, although Eurofer97 is a bit more stiff at lower temperatures. Nevertheless, this behavior might be expected due to characteristic microstructural features present in steel and alloying with 9% of Cr and other minor elements.

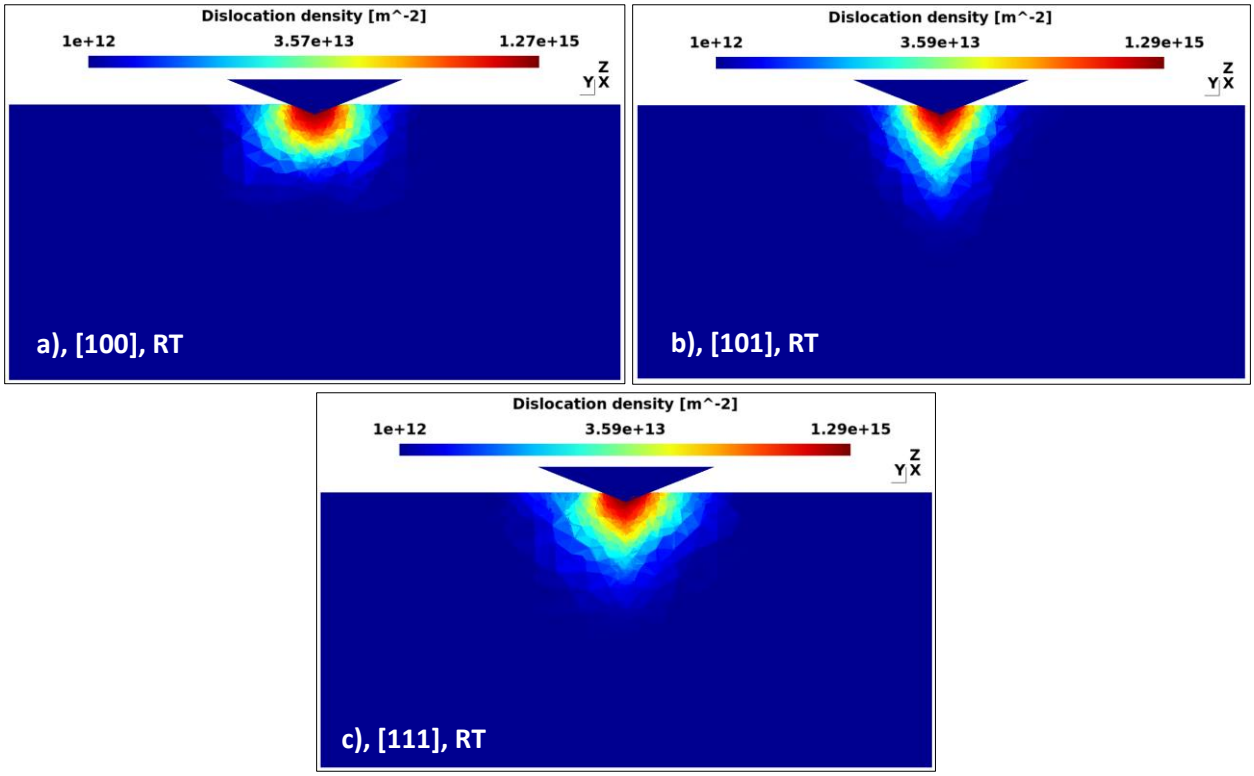

Figure 16. Dislocation density (log scale) at h = 1.5 µm and room temperature from FEA: a) [100] surface orientation, b) [101], c) [111].

The extension of the plastic deformation zone was also inspected by outputting the 2D profiles of the dislocation density underneath the indenter tip, in a similar way as it was experimentally studied by FIB-TEM. These profiles are presented in Figure 16. Here and on the following FEM pictures shown the X, Y and Z axes correspond to the illustration on Figure 3. A significant change of the dislocation density evolution pattern related to the test temperature was not found, so we show only the results obtained at room temperature. However, the pattern depends considerably on the crystal orientation of the indented surface and perspective view. Thereby, the dislocation density pattern evenly surrounds the indenter tip in a shape of a hemisphere in the case of the [100] surface orientation, as on Figure 16(a), whereas in the case of the [101] orientation, the plastic deformation extends into the bulk of the material, as on Figure 16(b). If the crystal surface orientation is [111], the dislocation density pattern appears to be a combination of the two other cases, experiencing the spherical distribution as in the [100], but still having a noticeable "peak" along the indentation direction, as shown in Figure 16(c).

By picking the absolute values of the dislocation density, we note that the density increase predicted by the CPFEM simulations agrees well with the TEM measurements (done in the sub-surface later yielding to $\approx 1\times10^{15}$ m^{-2} in experiment and to $\approx 1.3\times10^{15}$ m^{-2} in CPFEM). Of course the maximum dislocation density value is one of the constitutive parameters, which gives us a control on the dislocation density behavior, but the fact that it actually reaches this value and that it was obtained from the fitting to uniaxial tension tests, points on a good interconnection

between the crystal plasticity model and the real material behavior under both compressive and tensile deformations.

On Figure 17 we also provide the equivalent stress profiles, however calculated by means of crystal plasticity and not J_2 plasticity. In this case, the yielding of material does not happen according to the Von Mises yield criterion, but stress distributions must be precise. This is provided as a potential reference for similar works to be done on a nanoindentation response, but based on J_2 plasticity. Just as for the dislocation density patterns, the equivalent stress distribution profile does not change with the test temperature, but the overall stress level is decreasing from the highest value of 707 MPa at room temperature down to 278 MPa at 500°C, what can be seen in Figure 17(c, d, e). However, it changes with the crystal orientation and the stress distribution patterns are presented in Figure 17(a, b, c). One can see in Figure 17(a) that in the case of the [101] orientation, the stress propagates along Z axis as it happens with the dislocation density evolution and the highest values are accumulated below the indenter. If indentation is performed into the [100] orientation, as in Figure 17(c), stress behavior becomes the opposite – the highest and lowest stress concentrations are "mirrored" with respect to the [101] orientation. This happens because the [101] is achieved by rotation of the crystal lattice in [100] surface orientation by Euler angle θ on 45°, so the active slip systems co-rotate as well. The [111] orientation leads to an asymmetrical stress pattern if viewed from the same angle as shown in Figure 17(b). The stress propagates inside the bulk which is an expected behavior due to the fact that indenter is being immersed along the [111] slip direction in BCC metals. The symmetry of the stress distribution indeed it could be obtained by different in-plane surface orientation relative to the indenter, however, performing such dedicated configuration was not in the scope of our work, which primary focuses on the treatment of the experimental data, where the orientation of grains to indented axis is usually random.

It is important to emphasize that in the case of the [100] surface orientation, the highest stress is not concentrated right below the indenter tip, as in the case of the other two directions. Moreover, it has the lower values overall as can be seen by the comparison of color maps in Figure 17(a, b, c). This must be also related to the fact, that force-displacement curve for [100] surface orientation is always lower than the others, what can be seen in Figure 13(d).

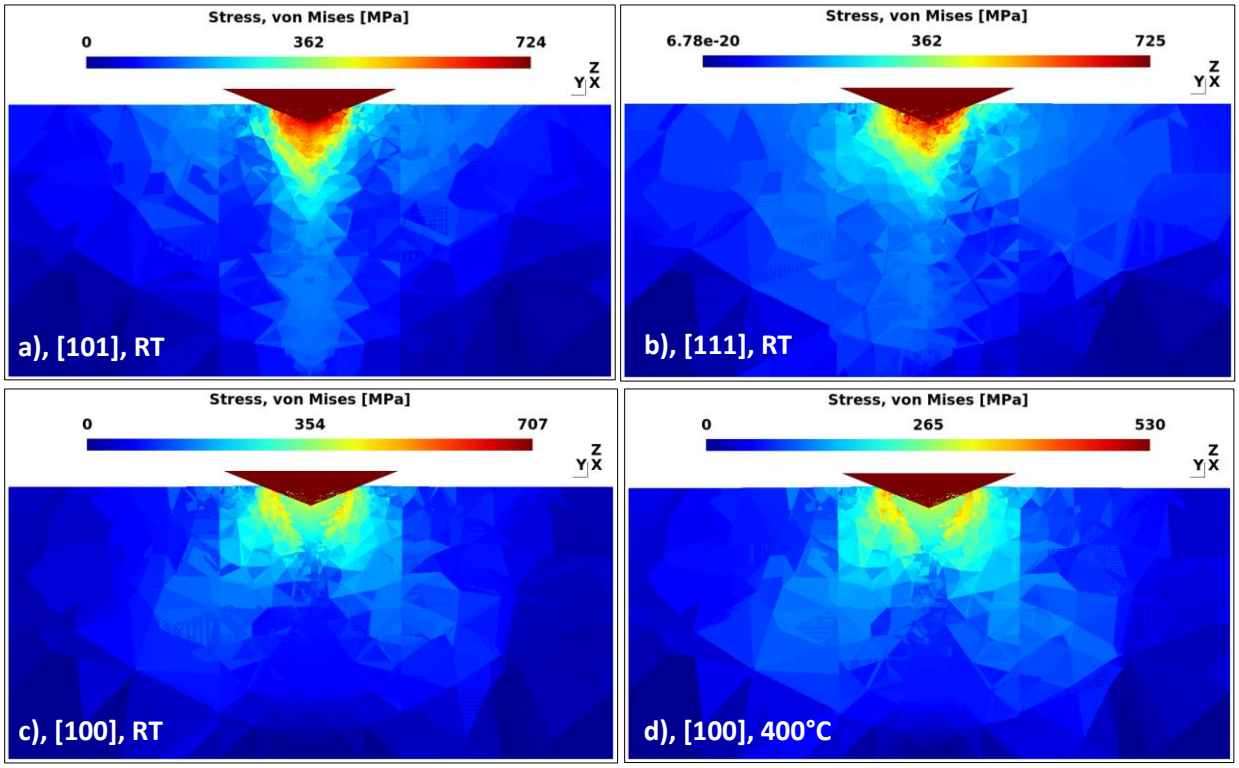

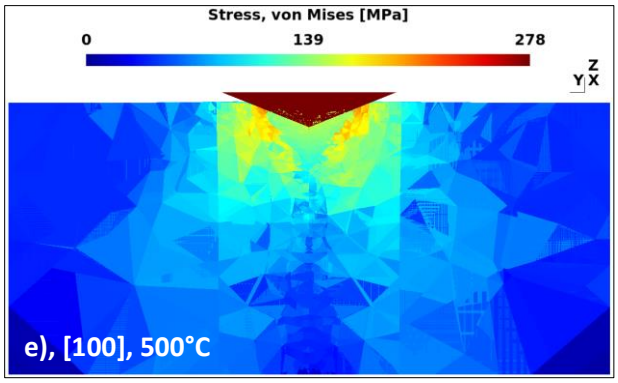

Figure 17. Von Mises equivalent stress at h_{max} for different grain orientations from FEA: a-c) room temperature; d) 400°C; e) 500°C;

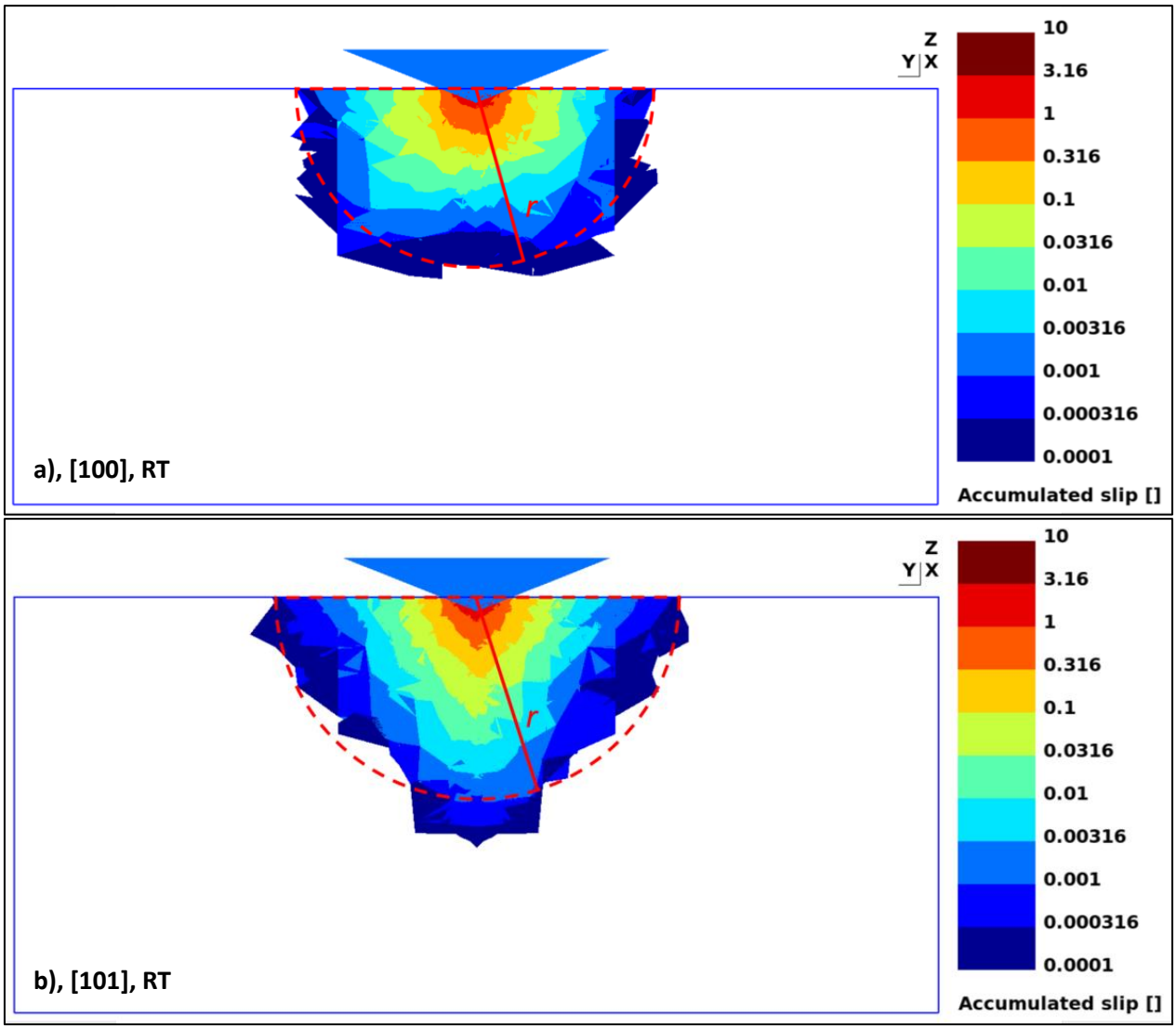

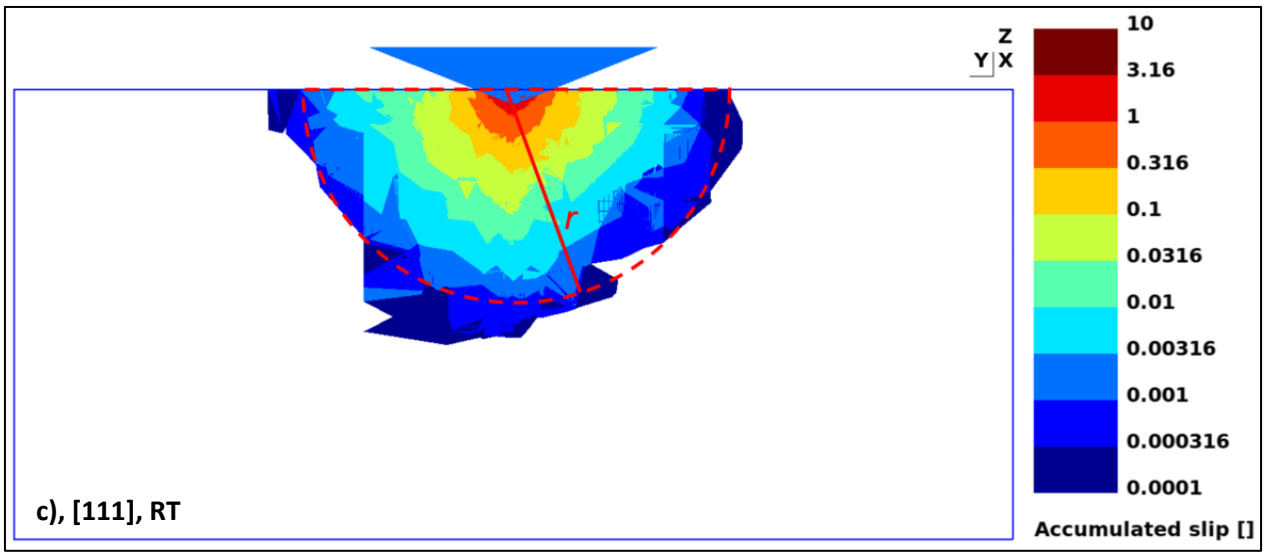

Figure 18. Accumulated slip (log scale) at h = 1.5 µm and room temperature from FEA: a) [100] surface orientation b) [101], c) [111].

Another common practice to explore the range of the plastic zone extension is to output the accumulated slip distribution. In Figure 18, we present the elements which undergo at least 0.01% deformation as accumulated slip (lower values do not extend the plastic zone further) which gives us an idea of plastic deformation region.. The radii of the obtained hemispheres with respect to the orientations were measured, and their ratios to the penetration depth of h = 1.5 µm were calculated and averaged as 13.82±0.8 µm. The radii of the hemispheres with respect to the temperature were measured also, however no significant difference was found in this case and the factor divergence for the [100] orientation was calculated as 2.5%. These facts allow us to conclude that the penetration depth to the plastic zone radius is constant for the studied material in this temperature range and only depends on the crystal orientation.

Previously we discussed the SEM and TEM inspection of the lamella obtained with FIB, where the ratio of h/r (see Figure 7 (b)) was found to be ≈5, and the formation of the dislocation bands indicated that this value must be higher. However, the deformation was estimated by analyzing the contrast fields obtained from different electron reactions and particular dislocation behavior. In the case of modelling, we can distinguish the elements experienced plastic deformation, therefore, more correctly estimate the plastic zone as well as accumulated slip gradients associated with the changes of the contrast otherwise seen by SEM tool. To demonstrate this approach, we superimpose the TEM micrograph and FEM accumulated slip color map as shown in Figure 19.

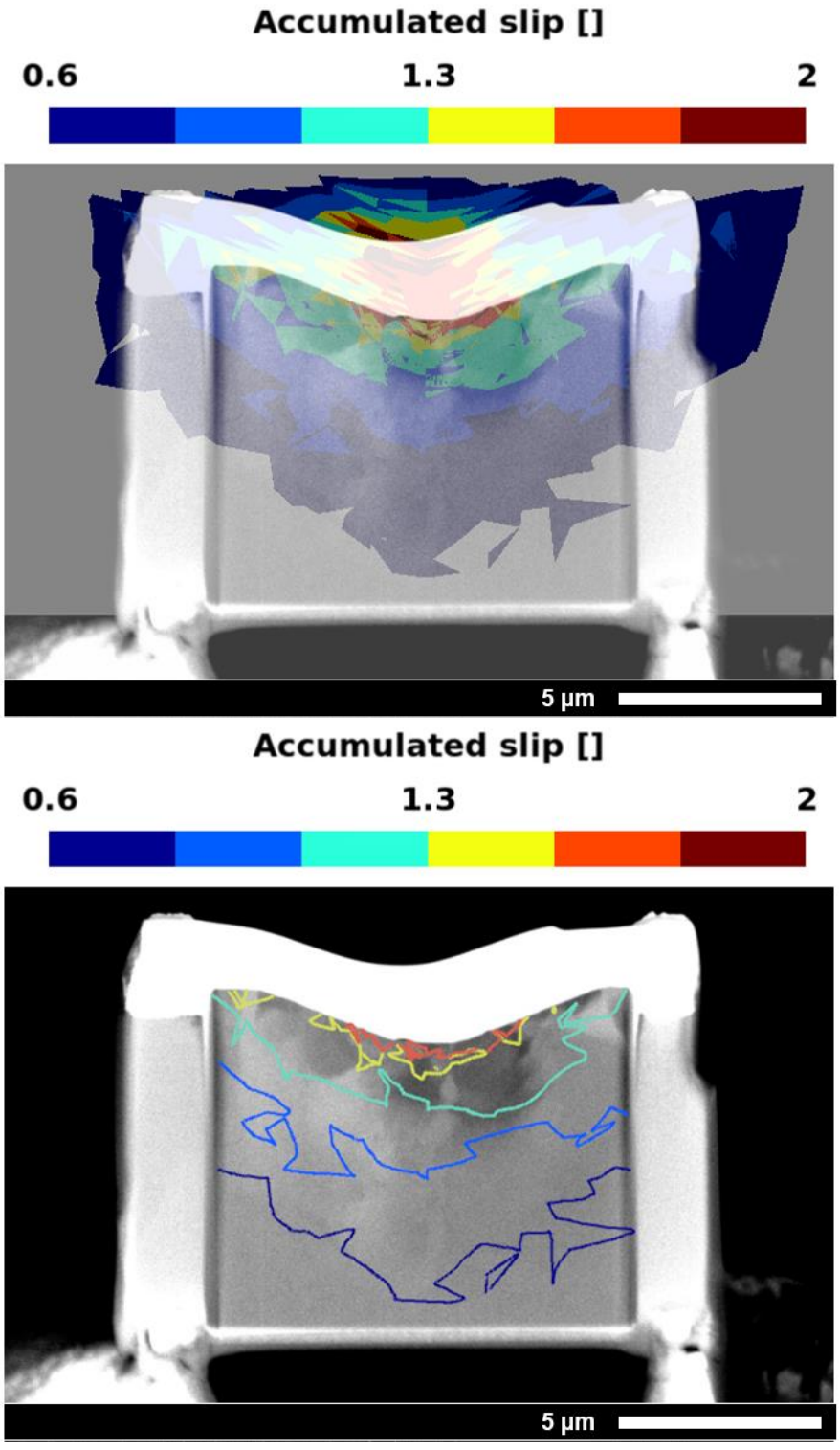

Figure 19. Plastic zones from FEA at RT and TEM compared by overlapping.

One can see that the deformation values of 60% and higher, precisely represent the contour of the SEM dark-light contrast in the lamella. The area of the lamella where the contrast is slightly inhomogeneous is reflected by the iso-lines corresponding to 0.6 and 0.83 of deformation. Zones experienced deeper deformation stay within 0.83 and

1.06, and the most dark-grey areas are at least 1.06 of deformation, with some particularly high deformed zones right next to the indenter tip of 1.3 and higher deformation values. Such approach provides a good understanding of the degree of the plastic deformation occurred in an each zone.

Our next step is to compare and discuss the formation of the pile-ups as observed experimentally and in CPFEM. By analyzing the orientations of the indented grains using EBSD maps, it was possible to retrieve the Euler angles and use them to similarly orient the crystal in CPFEM simulation. Figure 20(b, d, f) contains the following information: a picture of the lattice orientation obtained with the prescribed Euler angles (top left), the top view of the final nanoindentation imprint (top right) and the 3D picture of the imprint with the colormap (bottom). The transparent plane on the lattice orientation picture corresponds to the surface planes where indents were placed. Figure 20(a, c, e) shows the real indents taken by SEM.

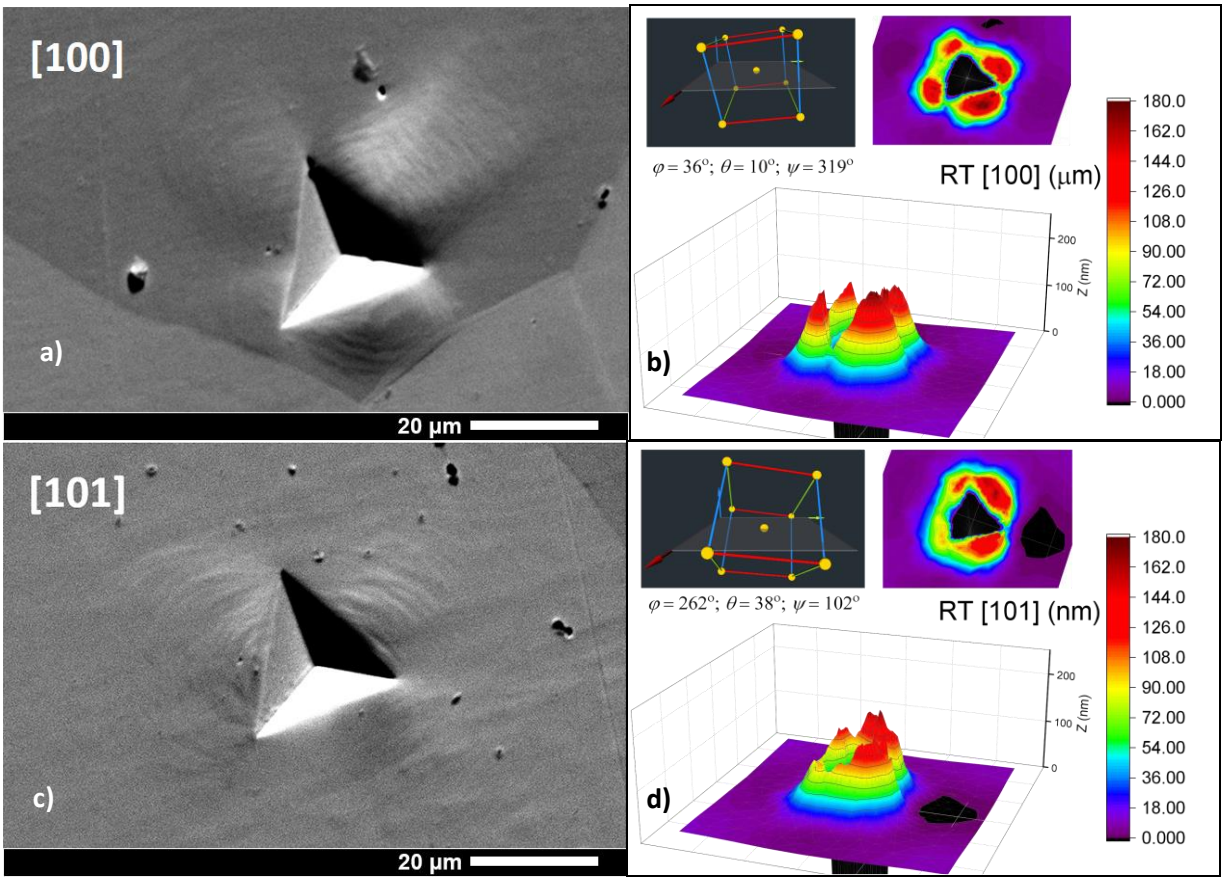

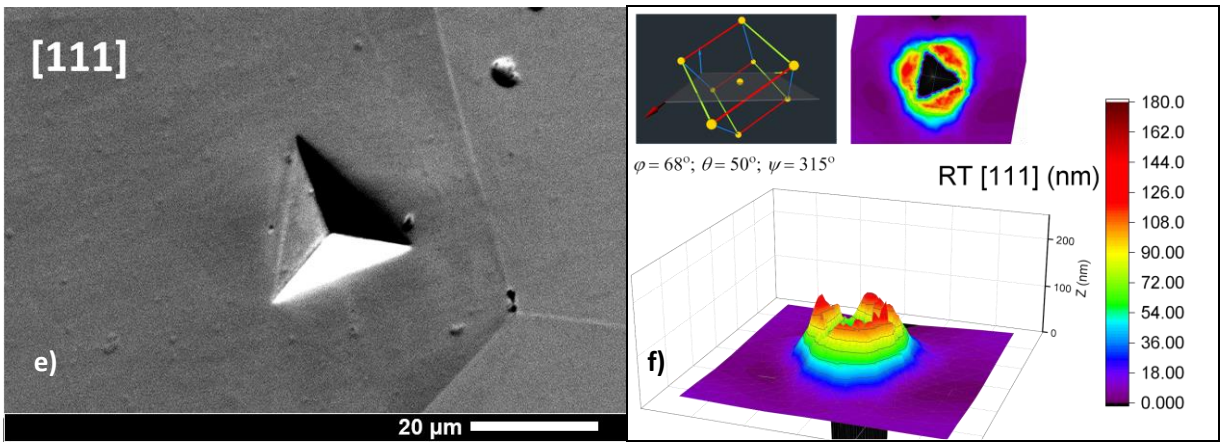

Figure 20. The final imprint and indentation pile-ups shapes taken from SEM and FEM.

One can note that the indent placed on the [100] and [101] surface orientations has two pile-ups, each created by one of the two sides of the Berkovich indenter and two adjacent ones both created by another side. In the case of CPFEM simulation, it looks like both indents have properly caught the pile-ups behavior, but in the case of [101] it's a topic of discussion if the height of each pile-up was correctly reproduced. Moreover, that the height of the experimental pile-up is impossible to precisely estimate using just SEM and proper investigation requires AFM for this.

The pile-ups in [111] surface orientation are hard to distinguish, but CPFEM seems to correctly reproduce this: overall pile-ups height is noticeably lower than in the other cases and very similar to each other.

4. Summary and conclusions

In summary, in this contribution we have applied the CP model in combination with FEM solver to simulate the nanoindentation process in BCC Fe in the range of temperatures from the room temperature up to 500°C. The constitutive laws for the CPFEM model were derived using the tensile deformation data and experimentally characterized microstructure (SEM-EBSD and TEM data) of that material. Thermal activation and strain rate dependence of the plastic slip has been introduced through the equations and parameterized by adopting the open literature data for BCC iron. After the nanoindentation, the dimensions of the imprints as well as profiles of the dislocation density around the indents were experimentally measured by means of scanning and transmission electron microscopy for the comparison with the predictions of the CPFEM model.

It was shown that the material behavior is properly caught by CPFEM setup, what is proven not only by the outcoming load-displacement curves, but also the stress distribution maps, accumulated slip distribution maps, associated dislocation density fields and the shape of final imprints represent the microstructural features in a good agreement with the results obtained using TEM and SEM, and correlate well with predictions done in other studies.

Hardness calculations are also in a good agreement with experimental values if obtained just by using the calculations for perfect indenter which we apply in the present simulations.

Despite of the good match between the experiments and CPFEM approach for the maximum applied force in the nanoindentation force-displacement curves, the initial force values appear to be significantly different (up to 60%). The reason for that can be a completely neglected friction in the model or a set of experimental artefacts. Another good explanation can be a fact, that the strain gradient theory is not introduced in the present model, so it affects the output curve at shallow depths, where the size effect is present, and therefore it affects the overall evolution of the force. It is possible to introduce the mentioned models into CPFEM, however non-linearity of differential equations will be growing with every new model implemented, hence raising up the computational demand.

To conclude, the set of the constitutive parameters defined from the tensile experiments is precise enough to reproduce true stress-strain curves of the studied material and in combination with presented CPFEM NI setup can also reproduce the nanoindentation F-d curves of the same material and testing conditions. The mathematical functional and CPFEM model are perfectly suitable for the incorporation of the irradiation defects (such as dislocation loops and voids) given that the thermally-activated dislocation-defect interaction can be parameterized based on the available theoretical and atomistic modelling studies.

Hence, the presented computational approach is a prospective tool to investigate the mechanical response of the material to the compressive deformation under nanoindentation experimental conditions. On the one hand, the approach adequately grasps the heterogeneity of the plastic deformation under indenter, and on the other hand it correctly transfers the constitutive law derived from the tensile tests. Importantly, the implemented computational approach remains rather flexible to introduce other sources alternating plastic deformation such as irradiation defects, effects of strain rate and temperature. In practice, this work is the first step towards the development of the CPFEM model which could treat the heterogeneous microstructure generated by the ion irradiation damage and thereby help to retrieve the local property of the material. In order to complete this model for ion irradiated steels one needs to apply and validate the model for BCC Fe with and without ion irradiation, update the model to treat non-irradiated F/M steel (to include specificity of the martensitic microstructure) and finally treat ion-irradiated F/M steel. The currently presented model includes all necessary functionality to include the F/M microstructure and to include the effect of ion irradiation. Therefore, within this contribution we provide thorough validation of the model including comparison with tensile data and detailed microstructural characterization.

Acknowledgment:

This work has been carried out within the framework of the EUROfusion Consortium, funded by the European Union via the Euratom Research and Training Programme (Grant Agreement No 101052200 — EUROfusion). Views and opinions expressed are however those of the author(s) only and do not necessarily reflect those of the European Union or the European Commission. Neither the European Union nor the European Commission can be held responsible for them.

References:

1. A. Zinkle, H. Muroga, S.J. Möslang, T. Tanigawa, Multimodal options for materials research to advance the basis for fusion energy in the ITER era, Nucl. Fusion 53 (2013) 104024.
2. E. Gaganidze, J. Aktaa, Assessment of neutron irradiation effects on RAFM steels, Fusion Engineering and Design 88, (2013) 118-128.
3. N. Singh, J.H. Evans, Significant differences in defect accumulation behavior between fcc and bcc crystals under cascade damage conditions, J. Nucl. Mater. 226 (1995) 277-285.
4. G. Federici, W. Biel, M.R. Gilbert, R. Kemp, N. Taylor, R. Wenninger, European DEMO design strategy and consequences for materials, Nucl. Fusion 57 (2017) 092002.
5. A. Prasitthipayong, D. Frazer, A. Kareer, M.D. Abad, A. Garner, B. Joni, T. Ungard, G. Ribarik, M. Preuss, L. Balogh, S.J. Tumey, A.M. Minora, P. Hosemann, Micro mechanical testing of candidate structural alloys for Gen-IV nuclear reactors, Nucl. Mater. and Energy 16 (2018) 34-45.
6. A. Ruiz-Moreno, P. Hähner, F. Fumagalli, V. Haiblikova, M. Conte, N. Randall, Stress−strain curves and derived mechanical parameters of P91 steel from spherical nanoindentation at a range of temperatures, Materials & Design 194 (2020) 108950.
7. P. Hosemann, C. Vieh, R.R. Greco, S. Kabra, J.A. Valdez, M.J. Cappiello, S.A. Maloy, Nanoindentation on ion irradiated steels, J. Nucl. Mater. 389 (2009), 239-247.
8. M. Saleh, Z. Zaidi, C. Hurt, M. Ionescu, P. Munroe, D. Bhattacharyya, Comparative Study of Two Nanoindentation Approaches for Assessing Mechanical Properties of Ion-Irradiated Stainless Steel 316, Metals 8 (2018), 719.
9. M. Saleh, Z. Zaidi, M. Ionescu, C. Hurt, K. Short, J. Daniels, P. Munroe, L. Edwards, D. Bhattacharyya, Relationship between damage and hardness profiles in ion irradiated SS316 using nanoindentation – Experiments and modelling, Int. J. Plast. 86 (2016), 151-169.
10. J.A. Knapp, D.M. Follstaedt, S.M. Myers, J.C. Barbour, T.A. Friedmann, Finite-element modeling of nanoindentation, J. App. Phys. 85 (1999).
11. J.A. Knapp, D.M. Follstaedt, J.C. Barbour, S.M. Myers, Finite-element modeling of nanoindentation for determining the mechanical properties of implanted layers and thin films, NIMB 127-128 (1997), 935-939.
12. B.D. Beake, A.J. Harris, J. Moghal, D. Armstrong, Temperature dependence of strain rate sensitivity, indentation size effects and pile-up in polycrystalline tungsten from 25 to 950 degrees, C. Materials & Design 156 (2018) 278-286.
13. X. Xiao, D. Terentyev, A. Ruiz, A. Zinovev, A. Bakaev, E.E. Zhurkin, High temperature nano-indentation of tungsten: Modelling and experimental validation. Mat Sci. Eng. a-Struct 743 (2019) 106-113.
14. A. Harris, B.D. Beake, D. Armstrong, M.I. Davies, Development of High Temperature Nanoindentation Methodology and its Application in the Nanoindentation of Polycrystalline Tungsten in Vacuum to 950°C, C. Exp. Mech. 57 (2017) 1115-1126.
15. E. Wyszkowska, L. Kurpaska, M. Frelek-Kozak, I. Jozwik, K. Perkowski, J. Jagielski, Investigation of the mechanical properties of ODS steels at high temperatures using nanoindentation technique. Nucl Instrum Meth B 444 (2019) 107-111.
16. D.H. Lee, I.C. Choi, G.H. Yan, Z.P. Lu, M. Kawasaki, U. Ramamurty, R. Schwaiger, J. Jang, Activation energy for plastic flow in nanocrystalline CoCrFeMnNi high-entropy alloy: A high temperature nanoindentation study, Scripta Materialia 156 (2018) 129-133.
17. I.C. Choi, C. Brandl, R. Schwaiger, Thermally activated dislocation plasticity in body-centered cubic chromium studied by high-temperature nanoindentation, Acta Materialia 140 (2017) 107-115.
18. D. Terentyev, X. Xiao, S. Lemeshko, U. Hangen, E.E. Zhurkin, High temperature nanoindentation of tungsten: Modelling and experimental validation. International Journal of Refractory Metals and Hard Materials 89 (2020) 105222.
19. M. Liu, C. Lu, A.K. Tieu, Crystal plasticity finite element method modelling of indentation size effect, International Journal of Solids and Structures 54 (2015) 42-49.
20. W.Z. Yao, J.H. You, Berkovich nanoindentation study of monocrystalline tungsten: a crystal plasticity study of surface pile-up deformation, Philosophical Magazine 97 (2017) 1418-1435.
21. M. Liu, A.K. Tieu, C. Peng, K. Zhou, Explore the anisotropic indentation pile-up patterns of single-crystal coppers by crystal plasticity finite element modelling, Mater. Letters 161 (2015) 227-230.

22. T. B. Britton, H. Liang, F. P. E. Dunne, A. J. Wilkinson, The effect of crystal orientation on the indentation response of commercially pure titanium: experiments and simulations, Proc. R. Soc. 466 (2010) 695-719.
23. Y. Aoyagi, S. Sakuma, Journal of the Society of Materials Science 64 (2015) 287-294.
24. Y. Su, C .Zambaldi, D. Mercier, P. Eisenlohr, T.R. Bieler, M.A. Crimp, Quantifying deformation processes near grain boundaries in α titanium using nanoindentation and crystal plasticity modeling, International Journal of Plasticity 86 (2016) 170-186.
25. X. Xiao, D. Terentyev, A. Ruiz, A. Zinovev, A. Bakaev, E.E. Zhurkin, High temperature nano-indentation of tungsten: Modelling and experimental validation, Materials Science and Engineering: A 743 (2019) 106-113.
26. X. Xiao, D. Terentyev, A. Bakaev, A. Zinovev, A. Dubinko, E.E. Zhurkin, Crystal plasticity finite element method simulation for the nano-indentation of plasma-exposed tungsten, J. Nucl. Mater. 518 (2019) 334-341.
27. P. Lin, J. Nie, M. Liu, Study on irradiation effect in stress-strain response with CPFEM during nano-indentation, Nucl. Mater. En. 22 (2020) 100737.
28. J. Nie, P. Lin, Y. Liu, H. Zhang, X. Wang, Simulation of the irradiation effect on hardness of Chinese HTGR A508-3 steels with CPFEM, Nucl. Eng. Techn. 51 (2019) 1970-1977.
29. J.P. Massoud, S. Bugat, B. Marini, D. Lidbury, S.V. Dyck, PERFECT – Prediction of Irradiation Damage Effects on Reactor Components: A summary, J. Nucl. Mat 406 (2010), 2-6.
30. C. Fazio, D.G. Briceno, M. Rieth, A. Gessi, J. Henry, L. Malerba, Innovative materials for Gen IV systems and transmutation facilities: The cross-cutting research project GETMAT, Nucl. Eng. Des. 241 (2011), 3514-3520.
31. L. Malerba, M.J. Caturla, E. Gaganidze, C. Kaden, M.J. Konstantinović, P. Olsson, C. Robertson, D. Rodney, A.M. Ruiz-Moreno, M. Serrano, J. Aktaa, N. Anento, S. Austin, A. Bakaev, J.P. Balbuena, F. Bergner, F. Boioli, M. Boleininger, G. Bonny, N. Castin, J.B.J. Chapman, P. Chekhonin, M. Clozel, B. Devincre, L. Dupuy, G. Diego, S.L. Dudarev, C.-C. Fu, R. Gatti, L. Gélébart, B. Gómez-Ferrer, D. Gonçalves, C. Guerrero, P.M. Gueye, P. Hähner, S.P. Hannula, Q. Hayat, M. Hernández-Mayoral, J. Jagielski, N. Jennett, F. Jiménez, G. Kapoor, A. Kraych, T. Khvan, L. Kurpaska, A. Kuronen, N. Kvashin, O. Libera, P.-W. Ma, T. Manninen, M.-C. Marinica, S. Merino, E. Meslin, F. Mompiou, F. Mota, H. Namburi, C.J. Ortiz, C. Pareige, M. Prester, R.R. Rajakrishnan, M. Sauzay, A. Serra, I. Simonovski, F. Soisson, P. Spätig, D. Tanguy, D. Terentyev, M. Trebala, M. Trochet, A. Ulbricht, M.Vallet, K. Vogel, T. Yalcinkaya, J. Zhao, Multiscale modelling for fusion and fission materials: The M4F project, Nucl. Mat. En. 29 (2021), 101051.
32. D. Terentyev, Yu.N. Osetsky, Competing processes in reactions between an edge dislocation and dislocation loops in a body-centred cubic metal, Scripta Materialia 62 (2010), 697-700.
33. L. Veleva, P. Hähner, A. Dubinko, T. Khvan, D. Terentyev, A. Ruiz-Moreno, Depth-Sensing Hardness Measurements to Probe Hardening Behaviour and Dynamic Strain Ageing Effects of Iron during Tensile Pre-Deformation, Nanomaterials 11 (2021) 71.
34. W.C. Oliver, G.M. Pharr, An improved technique for determining hardness and elastic modulus using load and displacement sensing indentation experiments, J. Mater. Res. 7 (1992) 1564 – 1583.
35. A.A. Volinsky, N.R. Moody, and W.W. Gerberich, J. Mater Res. 19 (2004) pp 2650-2657
36. H. Sakai, T. Tsuji, and K. Naito J. Nuclear Science and Technology, 21:11 (1984) 844-852
37. P.Y. Hour Oxidation of Metals and Alloys. In: J.A. Richardson et al. (eds.) Shreir's Corrosion, volume 1, pp. 195-239 (2010) Amsterdam: Elsevier.
38. Ellingham, H. J. T. (1944), "Reducibility of oxides and sulphides in metallurgical processes", J. Soc. Chem. Ind., London, 63 (5): 125.
39. C. Geuzaine, J.F. Remacle, Gmsh: A 3-D finite element mesh generator with built-in pre- and post-processing facilities, Int. J. for Numerical Methods in Engineering 79 (2009) 1309 – 1331.
40. G. Lemoine, L. Delannay, H. Idrissi, M.S. Colla, T. Pardoen, Dislocation and back stress dominated viscoplasticity in freestanding sub-micron Pd films, Acta materialia 111 (2016) 10-21.
41. F.X. Lin, M. Marteleur, P.J. Jacques, L. Delannay, Transmission of {332}< 113> twins across grain boundaries in a metastable β-titanium alloy, International Journal of Plasticity 105 (2018), 195-210.
42. U.F. Kocks, A.S. Argon, M.F. Ashby, Thermodynamics and kinetics of slip, 1975
43. H.J. Frost, M.F. Ashby, Deformation mechanism maps: the plasticity and creep of metals and ceramics, 1982.
44. F.R.N. Nabarro, One-dimensional models of thermal activation under shear stress, Phil. Mag. 83 (2003), 3047-3054.
45. K. Ono, Temperature Dependence of Dispersed Barrier Hardening, J. Appl. Phys. 39 (1968) 1803-1806.

46. E.O. Hall, The Deformation and Ageing of Mild Steel: III Discussion of Results, Proc. Phys. Soc. B 64 (1951) 747.
47. H. Mecking, U.F. Kocks, Kinetics of flow and strain-hardening, Acta Metallurgica 29 (1981) 1865 – 1875.
48. U.F. Kocks, Realistic constitutive relations for metal plasticity, Material Science and Engineering: A 317 (2001) 181-187.
49. E.B. Marin, P.R. Dawson, On modelling the elasto-viscoplastic response of metals using polycrystal plasticity, Computer Methods in Applied Mechanics and Engineering 165 (1998) 1-21.
50. F. Roters, P. Eisenlohr, T.R. Bieler, D. Raabe, Crystal Plasticity Finite Element Methods: In Materials Science and Engineering (2010).
51. X. Xiao, D. Song, J. Xue, H. Chu, H. Duan, A self-consistent plasticity theory for modeling the thermo-mechanical properties of irradiated FCC metallic polycrystals, Journal of the Mechanics and Physics of Solids 78 (2015) 1-16.
52. D. Terentyev, X. Xiao, A. Dubinko, A. Bakaeva, H. Duan, Dislocation-mediated strain hardening in tungsten: Thermo-mechanical plasticity theory and experimental validation, Journal of the Mechanics and Physics of Solids 85 (2015) 1-15.
53. G. I. Taylor, "Plastic Strain in Metals," Journal of the Institute of Metals, Vol. 62, 1938, pp. 307-324.
54. D. Kramer, H. Huang, M. Kriese, J. Robach, J. Nelson, A. Wright, D. Bahr, W.W. Gerberich, Yield strength predictions from the plastic zone around nanocontacts, Acta Materialia 47 (1998) 333-343.
55. P. Hosemann, D. Kiener, Y. Wang, S. A. Maloy, Issues to consider using nano indentation on shallow ion beam irradiated materials, Journal of Nuclear Materials 425 (2012) 136-139.
56. J. J. Adams, D. S. Agosta, R. G. Leisure, Elastic constants of monocrystal iron from 3 to 500K, Journal of Applied Physics 100 (2006) 113530.
57. W.P. Davey, Phys. Rev. 25 (1925).
58. K. Okazaki, Solid-solution hardening and softening in binary iron alloys, Journal of Materials Science 31 (1996) 1087 – 1099.
59. H.A. Khater, G. Monnet, D. Terentyev, A. Serra, Dislocation glide in Fe–carbon solid solution: From atomistic to continuum level description, Int. J. of Plasticity 62 (2014) 34-49.
60. N.A. Fleck, J.W. Hutchinson, A phenomenological theory for strain gradient effects in plasticity, J. Mech. Phys. Solids 41 (1993) 1825-1857.
61. ASTM E111-04(2010) Standard test method for Young's Modulus, Tangent Modulus, and Chord Modulus.
62. E. Gaganidze, F. Gillemot, I. Szenthe, M. Gorley, M. Rieth, E. Diegele, Development of EUROFER97 database and material property handbook, Fusion Engineering and Design 135(2018) 9-14.